

# Star formation in young star cluster NGC 1893

Saurabh Sharma,<sup>1\*</sup> A. K. Pandey,<sup>1,2</sup> D. K. Ojha,<sup>3</sup> W. P. Chen,<sup>2</sup> S. K. Ghosh,<sup>3</sup>  
B. C. Bhatt,<sup>4</sup> G. Maheswar<sup>1</sup> and Ram Sagar<sup>1</sup>

<sup>1</sup>*Aryabhata Research Institute of Observational Sciences (ARIES), Nainital 263 129, India*

<sup>2</sup>*Institute of Astronomy, National Central University, Chung-Li 32054, Taiwan*

<sup>3</sup>*Tata Institute of Fundamental Research, Mumbai 400 005, India*

<sup>4</sup>*CREST, Indian Institute of Astrophysics, Hosakote 562 114, India*

Accepted 2007 June 23. Received 2007 June 19; in original form 2007 April 20

## ABSTRACT

We present a comprehensive multiwavelength study of the star-forming region NGC 1893 to explore the effects of massive stars on low-mass star formation. Using near-infrared colours, slitless spectroscopy and narrow-band H $\alpha$  photometry in the cluster region we have identified candidate young stellar objects (YSOs) distributed in a pattern from the cluster to one of the nearby nebulae Sim 129. The  $V$ , ( $V - I$ ) colour–magnitude diagram of the YSOs indicates that majority of these objects have ages between 1 and 5 Myr. The spread in the ages of the YSOs may indicate a non-coeval star formation in the cluster. The slope of the  $K$ -band luminosity function for the cluster is estimated to be  $0.34 \pm 0.07$ , which agrees well with the average value ( $\sim 0.4$ ) reported for young clusters. For the entire observed mass range  $0.6 < M/M_{\odot} \leq 17.7$  the value of the slope of the initial mass function, ‘ $\Gamma$ ’, comes out to be  $-1.27 \pm 0.08$ , which is in agreement with the Salpeter value of  $-1.35$  in the solar neighbourhood. However, the value of ‘ $\Gamma$ ’ for pre-main-sequence phase stars (mass range  $0.6 < M/M_{\odot} \leq 2.0$ ) is found to be  $-0.88 \pm 0.09$  which is shallower than the value ( $-1.71 \pm 0.20$ ) obtained for main-sequence stars having mass range  $2.5 < M/M_{\odot} \leq 17.7$  indicating a break in the slope of the mass function at  $\sim 2 M_{\odot}$ . Estimated ‘ $\Gamma$ ’ values indicate an effect of mass segregation for main-sequence stars, in the sense that massive stars are preferentially located towards the cluster centre. The estimated dynamical evolution time is found to be greater than the age of the cluster, therefore, the observed mass segregation in the cluster may be the imprint of the star formation process. There is evidence for triggered star formation in the region, which seems to govern initial morphology of the cluster.

**Key words:** stars: formation – stars: luminosity function, mass function – stars: pre-main-sequence – open clusters and associations: individual: NGC 1893.

## 1 INTRODUCTION

Young open clusters provide important information relating to star formation process and stellar evolution, because such clusters contain massive stars as well as low-mass pre-main-sequence (PMS) stars. The age spread in a young open cluster represents the cluster formation time-scale which can be studied from the analysis of the colour–magnitude diagrams (CMDs) of very young open clusters. To understand the star formation process, it is necessary to know how the star formation proceeds in star clusters and whether the stellar mass distribution that arises from the fragmentation of molecular clouds is universal or depends on the local environments. Among various tools, the initial mass function (IMF) is one of the most

important tools to study the above-mentioned questions (cf. Pandey et al. 2005, and references therein).

An important study to explore the star formation history and IMF of young open clusters was by Phelps & Janes (1994), who observed 23 open clusters in the Cassiopeia region and estimated IMFs for eight young clusters (Phelps & Janes 1993). The slope of the upper mass part of the IMF was also systematically investigated by Massey and collaborators using the  $UBV$  CCD photometry and MK classification (Massey, Johnson & DeGioia-Eastwood 1995b; Massey et al. 1995a). They determined the IMF for various associations in the Galaxy and the Magellanic Clouds in a homogeneous manner and found no statistically significant difference in IMF slopes, with an average value of  $\Gamma = -1.1 \pm 0.1$  for stars having masses  $\gtrsim 7 M_{\odot}$ . Sagar et al. (1986) and Sagar & Richtler (1991) also made similar conclusions.

High-mass stars have strong influence on their nearby surroundings and can significantly affect the formation of low-mass stars.

\*E-mail: saurabh@aries.ernet.in

Recently, a relatively large number of low-mass stars have been detected in a few OB associations, e.g. Upper Scorpius, the  $\sigma$  and  $\lambda$  Ori regions (Preibisch & Zinnecker 1999; Dolan & Mathieu 2002). Since this realization, surveys have demonstrated that the IMFs must be essentially the same in all star-forming regions (e.g. Massey et al. 1995b; Hillenbrand 1997; Preibisch & Zinnecker 1999). The apparent difference is due mainly to the inherent low percentage of high-mass stars and the incomplete survey of low-mass stars in high-mass star-forming regions. Advancement in detectors along with various surveys such as the 2MASS (Two Micron All Sky Survey), DENIS (Deep Near-Infrared Southern Sky Survey) and *ISO* (*Infrared Space Observatory*) has permitted detailed studies of low-mass stellar population in regions of high-mass star formation.

The very young open cluster NGC 1893 (Massey et al. 1995b) is considered to be the centre of the Aur OB2 association. NGC 1893 can be recognized as an extended region of loosely grouped early-type stars, associated with the H II region IC 410 with two pennant nebulae, Sim 129 and 130 (Gaze & Shajn 1952), and obscured by several conspicuous dust clouds. NGC 1893 contains at least five O-type stars, two of which, HD 242908 and LS V +33° 16 (S3R2N15) are main-sequence (MS) O5 stars, and therefore younger than  $\sim 3$  Myr (Marco & Negueruela 2002).

*UBV* photometry of NGC 1893 has been presented by Hoag et al. (1961), Cuffey (1973), Moffat & Vogt (1974) and Massey et al. (1995b). Tapia et al. (1991) performed near-infrared (NIR) and Strömgen photometry for 47 stars in the field of the cluster. They estimated the age of the cluster as 4 Myr and derived a distance modulus  $(m - M)_0 = 13.18 \pm 0.11$  mag (4.3 kpc) and an extinction  $A_V = 1.68$  mag towards the cluster region. Strömgen photometry for 50 stars in the field of NGC 1893 has also been reported by Fitzsimmons (1993), who confirmed the distance and age found by Tapia et al. (1991). Vallenari et al. (1999) performed NIR photometry of the cluster and came to the conclusion that there could be many PMS candidates in NGC 1893, although their method did not allow clear discrimination from field interlopers. Cuffey (1973) derived  $E(B - V) = 0.4$  mag and distance = 3.6 kpc for the cluster. Marco, Bernabeu & Negueruela (2001) derived an average distance modulus  $V_0 - M_V = 13.9 \pm 0.2$  mag (6 kpc) and  $A_V = 1.42 \pm 0.13$  mag for the cluster, and also identified five emission-line stars as likely PMS members of NGC 1893. Recently, they identified 18 emission-line PMS stars in NGC 1893 region (Negueruela et al. 2007).

The detection of PMS objects in NGC 1893 is interesting because it is one of the youngest known open cluster and has a moderately large population of O-type stars, thus representing a good laboratory for the study of massive star formation and the impact of massive stars on the formation of lower mass stars (Marco & Negueruela 2002). In this paper, we present a multiwavelength study of the NGC 1893 to make a comprehensive exploration of the effects of massive stars on low-mass star formation. Deep optical *UBVRI* and narrow band  $H\alpha$  photometric data, slitless spectroscopy along with archival data from the surveys such as 2MASS, MSX (Midcourse Space Experiment), *IRAS* and NVSS (NRAO VLA Sky Survey) are used to understand the global scenario of star formation in the NGC 1893 region.

## 2 OBSERVATIONS AND DATA REDUCTION

### 2.1 Optical data

The CCD *UBV* (*RI*)<sub>c</sub> and  $H\alpha$ +continuum (cont.) photometric data were acquired on 2005 January 6 and 18, respectively, using the  $2048 \times 2048$  pixel CCD camera mounted on the *f*/13 Cassegrain

focus of the 104-cm Sampurnanand Telescope of Aryabhata Research Institute of Observational Sciences (ARIES), Nainital. In this set up, each pixel of the CCD corresponds to 0.37 arcsec and the entire chip covers a field of  $\sim 13 \times 13$  arcmin<sup>2</sup> on the sky. To improve the signal-to-noise (S/N) ratio, the observations were carried out in the binning mode of  $2 \times 2$  pixel. The full width at half-maximum (FWHM) of the star images were  $\sim 2$  arcsec. The read-out noise and gain of the CCD are  $5.3 e^-$  and  $10 e^-/\text{ADU}$ , respectively. The broadband *UBV* (*RI*)<sub>c</sub> observations were standardized by observing stars in the SA98 field (Landolt 1992) on 2005 January 7. The observed region of NGC 1893 is shown in Fig. 1 as the black square box and the log of the observations is given in Table 1. A blank field of  $\sim 13 \times 13$  arcmin<sup>2</sup> located at a distance of about  $1^\circ$  away towards east of the cluster was also observed to estimate the contamination due to foreground/background field stars.

The CCD data frames were reduced using computing facilities available at ARIES, Nainital. Initial processing of the data frames were done using the IRAF (Image Reduction and Analysis Facility)<sup>1</sup> and ESO-MIDAS (European Southern Observatory Munich Image Data Analysis System)<sup>2</sup> data reduction packages. Photometry of cleaned frames was carried out using DAOPHOT-II software (Stetson 1987). The point spread function (PSF) was obtained for each frame using several uncontaminated stars. Magnitudes obtained from different frames were averaged. When brighter stars were saturated on deep exposure frames, their magnitudes have been taken from short exposure frames. We used DAOGROW program for construction of an aperture growth curve required for determining the difference between aperture and profile fitting magnitude. Calibration of the instrumental magnitude to the standard system was done by using procedures outlined by Stetson (1992).

For translating the instrumental magnitude to the standard magnitude, the calibration equations derived using least-squares linear regression are as follows:

$$u = U + (7.004 \pm 0.004) - (0.005 \pm 0.006)(U - B) \\ + (0.431 \pm 0.005)X,$$

$$b = B + (4.742 \pm 0.005) - (0.035 \pm 0.004)(B - V) \\ + (0.219 \pm 0.004)X,$$

$$v = V + (4.298 \pm 0.002) - (0.038 \pm 0.002)(V - I) \\ + (0.128 \pm 0.002)X,$$

$$r = R + (4.202 \pm 0.004) - (0.046 \pm 0.007)(V - R) \\ + (0.078 \pm 0.003)X,$$

$$i = I + (4.701 \pm 0.004) - (0.059 \pm 0.003)(V - I) \\ + (0.044 \pm 0.003)X,$$

where  $U, B, V, R$  and  $I$  are the standard magnitudes and  $u, b, v, r$  and  $i$  are the instrumental aperture magnitudes normalized for 1 s of exposure time and  $X$  is the airmass. We have ignored the second-order colour correction terms as they are generally small in comparison to other errors present in the photometric data reduction. The typical DAOPHOT errors in magnitude and colour as a function of  $V$  magnitude are shown in Fig. 2, and statistical results

<sup>1</sup> IRAF is distributed by National Optical Astronomy Observatories, USA.

<sup>2</sup> ESO-MIDAS is developed and maintained by the European Southern Observatory.

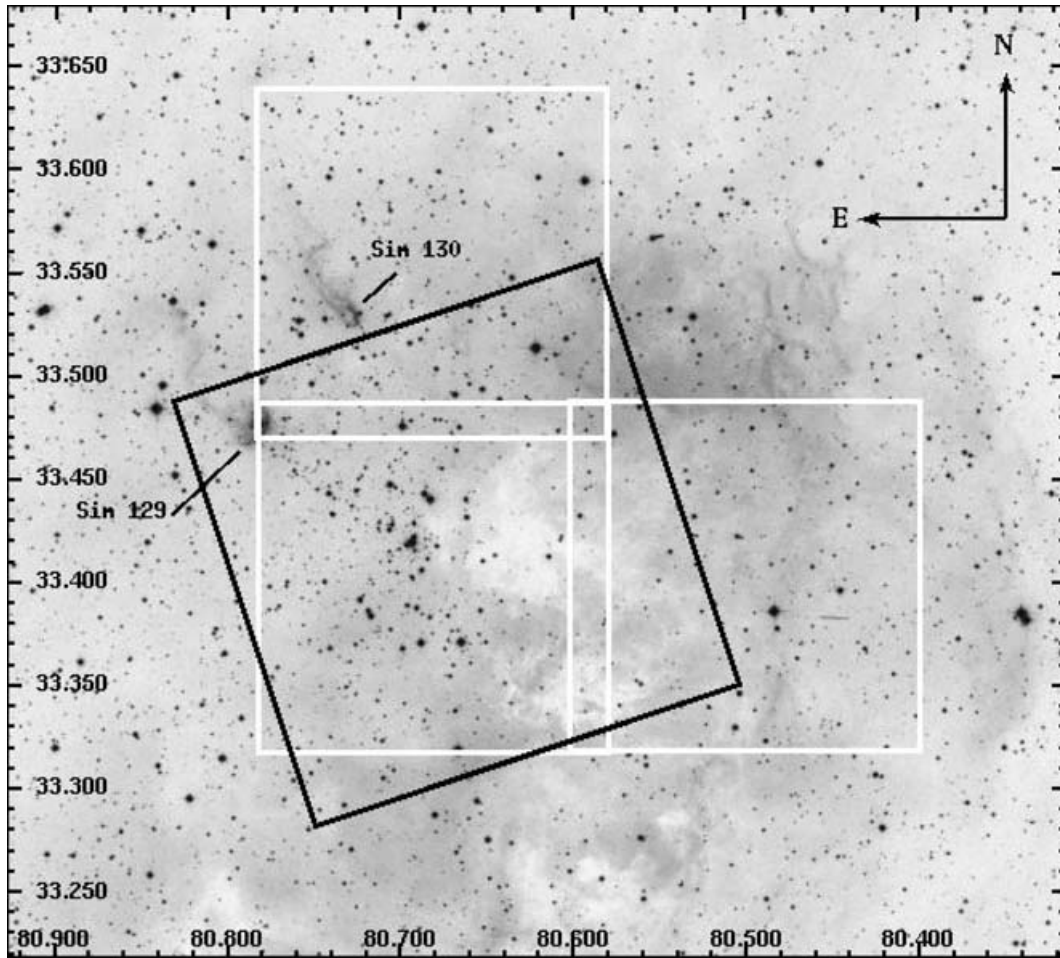


**Figure 1.** DSS image of the region around NGC 1893 cluster. The black square box represents the observed region of cluster in optical bands. The areas marked by the white boxes show the region of slitless spectroscopic observations. The  $x$  and  $y$  axes are RA and Dec. coordinates in degrees in J2000 epoch.

**Table 1.** Log of observation.

Date of observation/filter	Exp. (s) $\times$ No. of frames
Sampurnanand Telescope, ARIES	
2005 January 6	
$U$	$1200 \times 3, 900 \times 1, 300 \times 1, 120 \times 3$
$B$	$600 \times 4, 30 \times 3$
$V$	$600 \times 4, 30 \times 4$
$R_c$	$300 \times 4, 30 \times 1, 10 \times 4$
$I_c$	$300 \times 4, 30 \times 1, 10 \times 4$
2005 January 18	
$H\alpha$	$1200 \times 2, 300 \times 3, 60 \times 3$
Cont.	$1200 \times 2, 300 \times 3, 60 \times 3$
Himalayan <i>Chandra</i> Telescope, IIA	
2006 January 24	
Slitless spectra	$300 \times 9$
Direct frames	$60 \times 3$

are given in Table 2. The parameter  $\chi$  and sharpness are also shown in Fig. 2 as a function of  $V$  magnitude. It can be seen that the errors become large ( $\geq 0.1$  mag) for stars fainter than  $V \approx 22$  mag, so the measurements beyond this magnitude are not reliable. The standard deviations in the standardization residual,  $\Delta$ , between standard and transformed  $V$  magnitude and  $(U - B)$ ,  $(B - V)$ ,  $(V - R)$  and

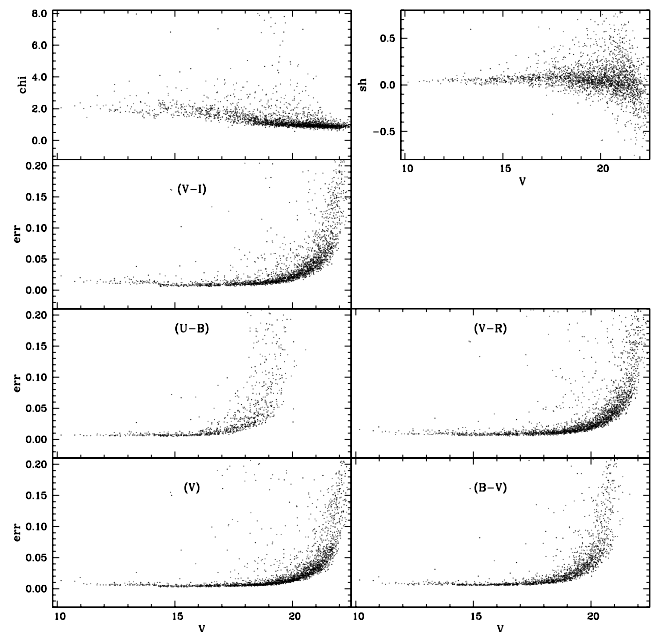


**Figure 2.** The DAOPHOT errors in magnitude and colours, image parameter  $\chi$  and sharpness as a function of  $V$  magnitude.

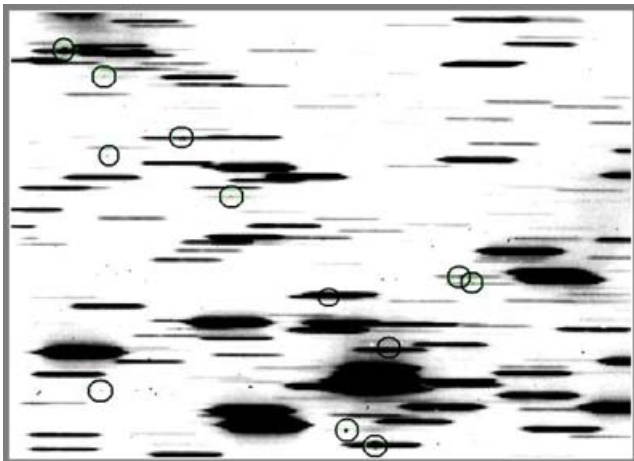
**Table 2.** Average photometric errors  $\sigma$  as a function of brightness.

V range (mag)	$\sigma_V$	$\sigma_{(U-B)}$	$\sigma_{(B-V)}$	$\sigma_{(V-R)}$	$\sigma_{(V-I)}$
10–11	0.01	0.01	0.01	0.02	0.02
11–12	0.01	0.01	0.01	0.01	0.01
12–13	0.01	0.01	0.01	0.01	0.01
13–14	0.01	0.01	0.01	0.01	0.01
14–15	0.01	0.01	0.01	0.01	0.01
15–16	0.01	0.01	0.01	0.01	0.01
16–17	0.01	0.01	0.01	0.01	0.01
17–18	0.01	0.03	0.01	0.01	0.01
18–19	0.01	0.04	0.02	0.02	0.01
19–20	0.02	0.07	0.04	0.02	0.02
20–21	0.03		0.06	0.04	0.04
21–22	0.05		0.08	0.06	0.06

$(V - I)$  colours of standard stars are 0.006, 0.025, 0.015, 0.010 and 0.015 mag, respectively.

## 2.2 Grism slitless spectroscopy

Three regions of the cluster (marked with white square boxes in Fig. 1) were also observed in the slitless mode with a grism as the dispersing element using the Himalayan Faint Object Spectrograph Camera (HFOSC) instrument on 2006 January 24. This yields an image where the stars are replaced by their spectra. A combination of a ‘wide  $H\alpha$ ’ interference filter (6300–6740 Å) and grism 5 (5200–10300 Å) of HFOSC was used without any slit. The resolution of grism is 870. The central  $2\text{ K} \times 2\text{ K}$  pixel of the  $2\text{ K} \times 4\text{ K}$  CCD were used for imaging. The pixel size is  $15\ \mu\text{m}$  with an image scale of  $0.297\ \text{arcsec pixel}^{-1}$ . For each region we secured three spectroscopic frames of 5-min exposure each with the grism in, and one direct frame of 1-min exposure with the grism out. Emission-line stars with enhancement over the cont. at  $H\alpha$  wavelength are visually identified. Fig. 3 shows the slitless spectra of stars in one of the cluster regions. Positions of the  $H\alpha$  emission stars are given in Table 3. Recently, Negueruela et al. (2007) have reported detection of 18  $H\alpha$  emission stars, of which 12 lies in the region surveyed by us. However, only nine stars are common in both the surveys.

**Figure 3.** One of the slitless spectra of the cluster region. The  $H\alpha$  emission line sources have been marked by circles.**Table 3.** Position of all the  $H\alpha$  emission stars.

ID	Slitless spectroscopy		ID	Narrow-band photometry	
	RA (2000) ( <sup>h</sup> : <sup>m</sup> : <sup>s</sup> )	Dec. (2000) ( <sup>o</sup> : <sup>'</sup> : <sup>''</sup> )		RA (2000) ( <sup>h</sup> : <sup>m</sup> : <sup>s</sup> )	Dec. (2000) ( <sup>o</sup> : <sup>'</sup> : <sup>''</sup> )
A	05:22:43.02	+33:25:05.4	a	05:22:19.86	+33:22:14.2
B	05:22:43.78	+33:25:25.8	b	05:22:19.90	+33:21:32.5
C	05:22:45.78	+33:28:16.2	c	05:22:22.41	+33:20:18.0
D	05:22:46.08	+33:24:57.8	d	05:22:27.64	+33:20:13.5
E	05:22:49.57	+33:30:01.5	e	05:22:30.67	+33:19:27.1
F	05:22:51.04	+33:25:47.1	f	05:22:31.14	+33:22:58.9
G	05:22:51.90	+33:23:59.3	g	05:22:31.92	+33:29:05.7
H	05:22:52.23	+33:29:58.0	h <sup>a</sup>	05:22:43.02	+33:25:05.4
I	05:22:52.30	+33:24:07.4	i <sup>a</sup>	05:22:43.78	+33:25:25.8
J	05:22:56.42	+33:26:47.7	j	05:22:46.84	+33:29:28.1
K	05:22:58.10	+33:30:41.0	k <sup>a</sup>	05:22:49.57	+33:30:01.5
L	05:22:58.85	+33:28:34.6	l	05:22:51.23	+33:20:35.5
M	05:22:59.57	+33:27:32.5			
N	05:23:00.07	+33:30:39.0			
O	05:23:02.87	+33:28:17.8			
P	05:23:04.26	+33:28:46.4			

<sup>a</sup>Also detected in slitless spectroscopy.

## 2.3 $H\alpha$ photometry

The excess  $H\alpha$  emission stars may also be detected by imaging the cluster region in  $H\alpha$  line and a nearby cont. (see e.g. Sung, Chun & Bessell 2000). We calculated the difference  $\Delta = (H\alpha_{\text{instrumental}} - \text{cont.}_{\text{instrumental}})$  and designated a star having excess emission if  $\Delta$  is greater than  $3\sigma$  from the mean value of the distribution in the  $H\alpha/\text{cont.}$  diagram. In Fig. 4, we have plotted  $H\alpha/\text{cont.}$ ,  $(H\alpha - \text{cont.})/(V - I)$  and  $V/(H\alpha - \text{cont.})$  diagrams. Probable  $H\alpha$  emission stars are shown by open circles. Information about photometrically detected  $H\alpha$  emission stars is given in Table 3. Only three probable photometrically detected  $H\alpha$  emission stars are common with those detected by the slitless spectroscopy. Here it is worthwhile to point out that some late-type dwarfs show strong chromospheric  $H\alpha$  in emission. Huang, Chen & Hsiao (2006) have pointed out that, even if a late-type star does not show  $H\alpha$  emission, such a star generally has a series of strong metal oxide absorption lines, such as TiO in its spectrum. This may lead to an underestimation of their cont., hence making the star as an  $H\alpha$  emitter.

## 3 OTHER AVAILABLE DATA SETS

NIR ( $JHK_s$ ) data for point sources around the cluster region have been obtained from the 2MASS Point Source Catalog (PSC). The 2MASS data base provides photometry in the NIR  $J$  ( $1.25\ \mu\text{m}$ ),  $H$  ( $1.65\ \mu\text{m}$ ) and  $K_s$  ( $2.17\ \mu\text{m}$ ) bands to a limiting magnitude of 15.8, 15.1 and 14.3, respectively, with a S/N ratio greater than 10. We retain only those sources for which the error in each band is less than 0.1 mag to ensure good photometric accuracy.

The MSX surveyed the Galactic plane in four mid-infrared (MIR) bands –  $A$  ( $8.28\ \mu\text{m}$ ),  $C$  ( $12.13\ \mu\text{m}$ ),  $D$  ( $14.65\ \mu\text{m}$ ) and  $E$  ( $21.34\ \mu\text{m}$ ) at a spatial resolution of  $\sim 18\ \text{arcsec}$  (Price et al. 2001). Two of these bands ( $A$  and  $C$ ) with  $\lambda(\Delta\lambda)$  corresponding to  $8.28(3.36)$  and  $12.13(1.71)$  include several unidentified infrared emission bands (UIBs) at 6.2, 7.7, 8.7, 11.3 and  $12.7\ \mu\text{m}$ . MSX images in these four bands around the cluster region were used to study the emission from the UIBs and to estimate the spatial distribution of temperature and optical depth of warm interstellar dust.

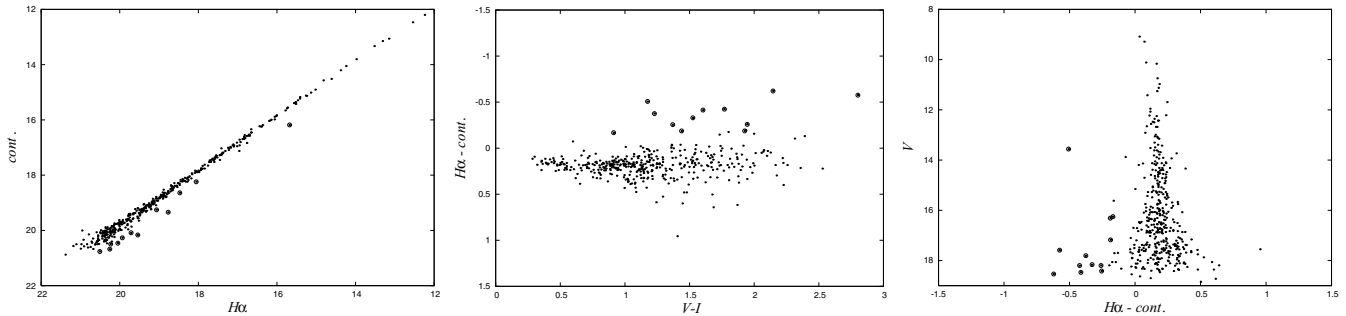


**Figure 4.** Left panel:  $H\alpha$  versus cont. diagram; middle panel:  $(H\alpha - \text{cont.})$  versus  $(V - I)$  diagram; right panel:  $V$  versus  $(H\alpha - \text{cont.})$  diagram. Circle represents probable  $H\alpha$  emission stars.

**Table 4.** List of *IRAS* point sources.

<i>IRAS</i> PSC	RA (2000)	Dec. (2000)	$F_{12}$	$F_{25}$	$F_{60}$	$F_{100}$
	( $^{\circ}$ )	( $^{\circ}$ )	(Jy)	(Jy)	(Jy)	(Jy)
05186+3326	80.4944	33.4943	1.47	2.12	22.95	146.60
05189+3327	80.5674	33.5059	1.31	2.06	46.35	120.50
05194+3322	80.6848	33.4240	1.16	1.38	2.29	29.48
05196+3329	80.7390	33.5326	1.08	2.39	28.30	163.40
05198+3325	80.7844	33.4771	8.33	26.16	145.70	163.40
05200+3329	80.8315	33.5299	1.39	1.91	145.70	163.40

The data from the *IRAS* survey around the cluster region in the four bands (12, 25, 60, 100  $\mu\text{m}$ ) were HIRES processed (Aumann, Fowler & Melnyk 1990) to obtain high angular resolution maps. These maps were used to determine the spatial distribution of dust colour temperature and optical depth. Six *IRAS* point sources have also been identified in the cluster region and their details are given in Table 4.

#### 4 COMPARISON WITH PREVIOUS STUDIES

We have carried out a comparison of the present photometric data with those available in the literature. The difference  $\Delta$  (literature – present data) as a function of  $V$  magnitude is shown in Fig. 5, and the statistical results are given in Table 5. The comparison indicates that the present photometry is in agreement with the CCD photometry by Massey et al. (1995b) and photoelectric (PE) photometry by Hoag et al. (1961). The  $(B - V)$  and  $(U - B)$  colours by Cuffey (1973) are

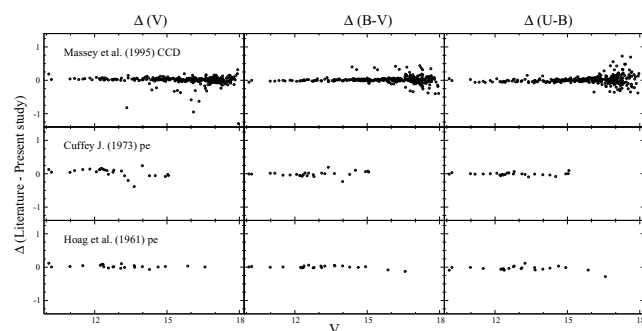


**Figure 5.** Comparison of present data with those given in literature. The difference ( $\Delta = \text{present study} - \text{literature}$ ) is plotted as a function of  $V$  magnitude.

in agreement with the present photometry whereas the  $\Delta V$  shows some variation.

#### 5 COMPLETENESS OF THE DATA

To study the luminosity function (LF)/mass function (MF) it is very important to make necessary corrections in data sample to take into account the incompleteness that may occur for various reasons (e.g. crowding of the stars). We used the ADDSTAR routine of DAOPHOT-II to determine the completeness factor (CF). The procedures have been outlined in detail in our earlier work (Sagar & Richtler 1991; Pandey, Ogura & Sekiguchi 2000; Pandey et al. 2001). In the case of optical CCD photometry the incompleteness of the data increases with increasing magnitude as expected. The CF as a function of  $V$  magnitude is given in Table 6. In the case of 2MASS the data are found to be almost complete up to 14 mag in the  $K_s$  band.

#### 6 STRUCTURE OF THE CLUSTER

##### 6.1 Isodensity contours

The initial stellar distribution in star clusters may be governed by the structure of parental molecular cloud and also how star formation proceeds in the cloud (Chen et al. 2004; Sharma et al. 2006). Later evolution of the cluster may be governed by internal gravitational interaction among member stars and external tidal forces due to the Galactic disc or giant molecular clouds.

To study the morphology of the cluster, we have generated isodensity contours (Fig. 6) for stars from optical ( $V \leq 18$ ) as well as from NIR 2MASS data. The contours are plotted above the  $3\sigma$  value of the background level as estimated from the control field. The filled square and circle marked in Fig. 6 represent the location of the nebula Sim 129 and cluster centre (as estimated in next section), respectively. The isodensity contours indicate that the cluster has elongated morphology.

##### 6.2 Radial density profile

To estimate the radial extent of the cluster we assume a spherical symmetry for the cluster. The centre of the cluster is determined using the stellar density distribution of stars having  $V \leq 20$  mag, in a  $\pm 100$ -pixel wide strip along both  $x$  and  $y$  directions around an initially eye estimated centre. The point of maximum density

**Table 5.** Comparison of the present photometry with the available photometry in the literature. The difference  $\Delta$ (literature – present data) is in magnitude. Mean and  $\sigma$  are based on  $N$  stars in a  $V$  magnitude bin.

$V$ range (mag)	$\Delta(V)$ (mean $\pm \sigma$ )	$N$	$\Delta(B - V)$ (mean $\pm \sigma$ )	$N$	$\Delta(U - B)$ (mean $\pm \sigma$ )	$N$
Massey P. et al. (1995a, CCD)						
10–11	0.033 $\pm$ 0.010	2	–0.012 $\pm$ 0.016	2	0.006 $\pm$ 0.022	2
11–12	0.042 $\pm$ 0.020	6	–0.010 $\pm$ 0.010	6	–0.045 $\pm$ 0.022	6
12–13	0.036 $\pm$ 0.027	16	–0.003 $\pm$ 0.021	16	–0.022 $\pm$ 0.033	16
13–14	0.035 $\pm$ 0.040	16	0.001 $\pm$ 0.022	16	–0.012 $\pm$ 0.051	16
14–15	0.020 $\pm$ 0.075	43	0.029 $\pm$ 0.077	43	–0.010 $\pm$ 0.030	43
15–16	0.003 $\pm$ 0.092	55	0.024 $\pm$ 0.070	54	0.015 $\pm$ 0.038	53
16–17	–0.003 $\pm$ 0.074	109	0.032 $\pm$ 0.087	109	0.015 $\pm$ 0.103	106
17–18	0.004 $\pm$ 0.010	73	0.015 $\pm$ 0.136	73	0.023 $\pm$ 0.189	71
Cuffey J. (1973, PE)						
10–11	0.043 $\pm$ 0.004	2	0.002 $\pm$ 0.020	2	0.017 $\pm$ 0.021	2
11–12	0.120 $\pm$ 0.024	3	–0.023 $\pm$ 0.034	3	–0.005 $\pm$ 0.006	3
12–13	0.095 $\pm$ 0.052	10	–0.036 $\pm$ 0.036	10	–0.005 $\pm$ 0.036	10
13–14	–0.064 $\pm$ 0.244	5	–0.004 $\pm$ 0.151	5	–0.033 $\pm$ 0.038	5
14–15	–0.066 $\pm$ 0.014	3	0.049 $\pm$ 0.062	3	–0.042 $\pm$ 0.043	3
15–16	–0.035 $\pm$ 0.023	2	0.063 $\pm$ 0.019	2	0.049 $\pm$ 0.066	2
Hoag et al. (1961, PE)						
10–11	0.013 $\pm$ 0.010	2	0.007 $\pm$ 0.016	2	–0.008 $\pm$ 0.001	2
11–12	0.047 $\pm$ –	1	0.006 $\pm$ –	1	–0.037 $\pm$ –	1
12–13	0.033 $\pm$ 0.042	7	0.004 $\pm$ 0.032	7	–0.036 $\pm$ 0.044	7
13–14	0.020 $\pm$ 0.048	6	0.030 $\pm$ 0.022	6	–0.018 $\pm$ 0.070	6
14–15	–0.017 $\pm$ 0.047	3	0.002 $\pm$ 0.011	3	0.003 $\pm$ 0.032	3

**Table 6.** CF of photometric data in the cluster and field regions.

$V$ range (mag)	NGC 1893		Field region
	$r \leq 2'$	$2' < r \leq 6'$	
10–11	1.00	1.00	1.00
11–12	1.00	1.00	1.00
12–13	1.00	1.00	1.00
13–14	1.00	1.00	1.00
14–15	1.00	1.00	1.00
15–16	1.00	1.00	1.00
16–17	1.00	1.00	1.00
17–18	1.00	1.00	1.00
18–19	0.95	1.00	1.00
19–20	0.96	0.93	0.96
20–21	0.68	0.65	0.68

obtained by fitting a Gaussian curve is considered as the centre of the cluster. The  $(x, y)$  pixel coordinates of the cluster centre are found to be (585, 394) which corresponds to  $\alpha_{2000} = 05^{\text{h}}22^{\text{m}}49^{\text{s}}$ ,  $\delta_{2000} = 33^{\circ}25'35''$ .

To determine the radial surface density we divided the cluster into a number of concentric circles. Projected radial stellar density in each concentric annulus was obtained by dividing the number of stars in each annulus by its area and the same are plotted in Fig. 7 for various magnitude levels. The error bars are derived assuming that the number of stars in a concentric annulus follows the Poisson statistics. The horizontal dashed line in the plot indicates the density of contaminating field stars, which is obtained from the region  $\sim 1^{\circ}$  away towards east of the cluster centre.

To check whether the density distribution shown in the left-hand panel of Fig. 7 is affected by contamination due to field stars, we

selected a sample of stars near a well-defined MS in the CMD as mentioned by Pandey et al. (2001). The radial density distribution of the MS sample is also shown in the right-hand panel of Fig. 7. Both the samples in general show almost similar radial density profiles. We have also used 2MASS data to obtain the radial density profile of the cluster and the same is shown in Fig. 7 (bottom panels), which also shows a similar radial density profile.

We have used these profiles to calculate the extent of cluster ' $r_{\text{cl}}$ ' which is defined as the point at which the radial density becomes constant and merges with the field density. The radial distribution of stars shown in Fig. 7 indicates that in general the extent of NGC 1893 cluster is  $\sim 6$  arcmin (5.7 pc).

To parametrize the radial density profiles we follow the approach by Kaluzny & Udalski (1992). Because of the low S/N ratio in the star counts of open clusters, it is not an easy task to constrain the tidal radius of cluster using the empirical model of King (1962). We describe radial density  $\rho(r)$  as

$$\rho(r) \propto \frac{f_0}{1 + (r/r_c)^2},$$

where  $r_c$  is the core radius (the radius at which the surface density falls to half of the central density  $f_0$ ). We fit above function to the observed radial density profile of stars. The best fit is obtained by  $\chi^2$  minimization technique. The fit was performed for the data within the radii of 10 arcmin.

The core radius for various magnitude levels ( $14 \leq V \leq 20$ ) varies from  $1.1 \pm 0.2$  arcmin ( $\sim 1.0 \pm 0.2$  pc) to  $2.6 \pm 0.7$  arcmin ( $\sim 2.5 \pm 0.7$  pc), whereas for MS stars it varies from  $1.0 \pm 0.2$  arcmin ( $\sim 1.0 \pm 0.2$  pc) to  $2.8 \pm 0.6$  arcmin ( $\sim 2.6 \pm 0.6$  pc). The 2MASS data give a core radius as  $1.6 \pm 0.6$  arcmin ( $\sim 1.5 \pm 0.6$  pc) for both the samples. To study the CMDs, MF etc. in detail, we divided the

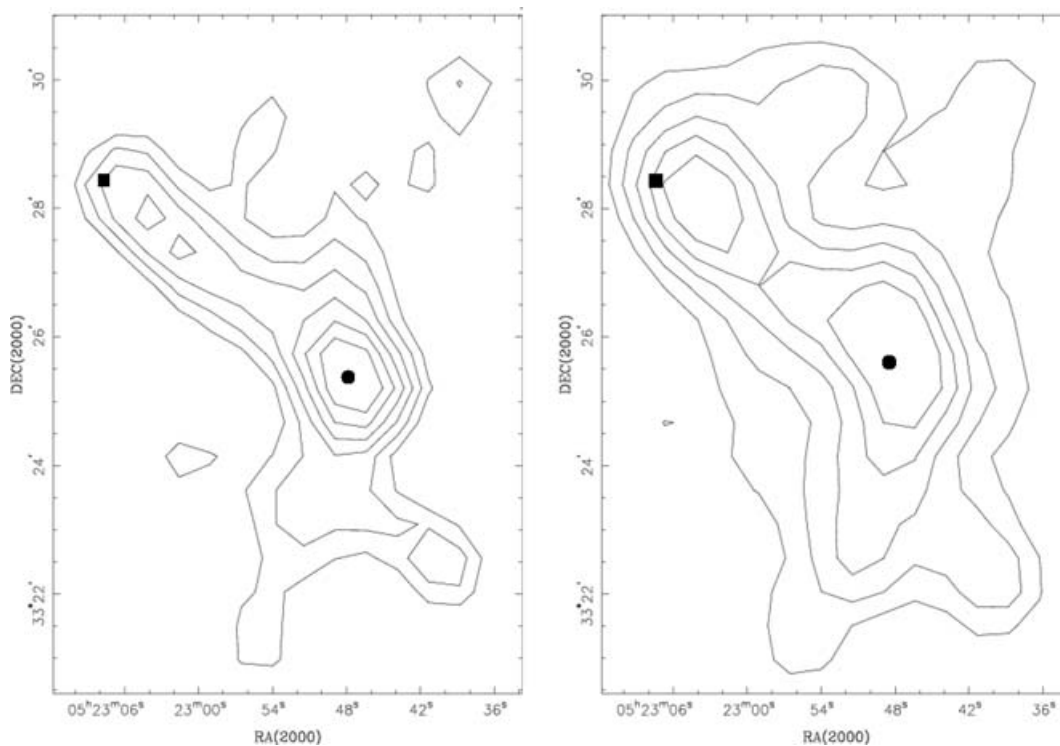


**Figure 6.** Isodensity contours for (a) stars having  $V \leq 18$  mag; (b) 2MASS stars in  $K_s$  band. The contours are plotted above  $3\sigma$  levels. For optical data, the contours have step size of  $1 \text{ star pc}^{-2}$  with the lowest contour representing  $5 \text{ stars pc}^{-2}$ . The maximum stellar density is  $12 \text{ stars pc}^{-2}$ . For 2MASS data, the contours have step size of  $2 \text{ stars pc}^{-2}$  with lowest contour representing  $6 \text{ stars pc}^{-2}$ . The maximum stellar density is  $18 \text{ stars pc}^{-2}$ . The filled square and circle represent the locations of nebula Sim 129 and cluster centre.

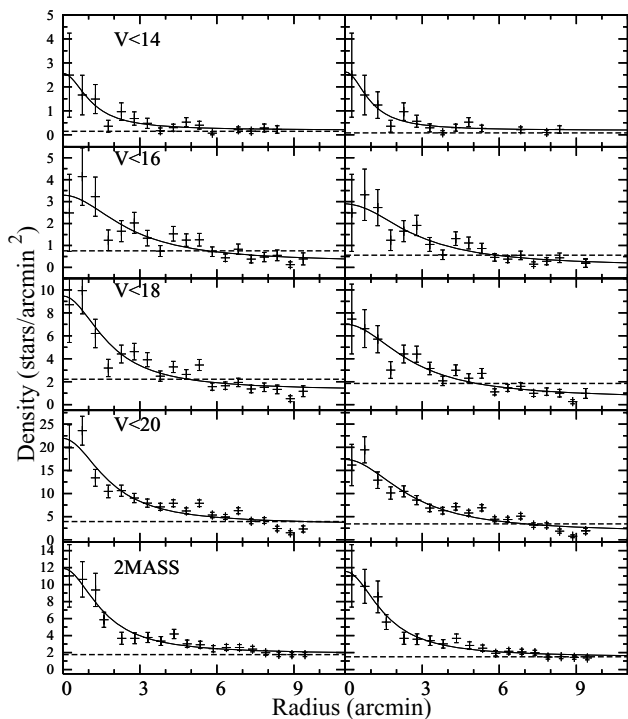


**Figure 7.** The radial density profiles of the cluster NGC 1893 for different optical magnitude levels and 2MASS data (in  $K_s$  band) for all (left-hand panels) and MS (right-hand panels) stars. The solid curve shows a least-square fit of the King (1962) profile to the observed data points. The error bars represent  $\pm\sqrt{N}$  errors. The dashed line indicate the density of field stars.

cluster into two subregions as the inner region ( $r < 2$  arcmin,  $1.9 \text{ pc}$ ), and the outer region ( $2 \leq r \leq 6$  arcmin,  $1.9 \leq r \leq 5.7 \text{ pc}$ ).

## 7 INTERSTELLAR EXTINCTION

### 7.1 Reddening

The extinction towards the cluster region is estimated using the  $(U - B)/(B - V)$  two-colour diagram (TCD) shown in Fig. 8, where the MS (Schmidt-Kaler 1982) is shifted along the reddening vector having an adopted slope of  $E(U - B)/E(B - V) = 0.72$  to match the observations. The TCD shows a spread in the observed sequence indicating the presence of differential reddening which is an indication of the youth of the cluster. Fig. 8 yields a spread in reddening between  $E(B - V) = 0.4$  and  $0.6 \text{ mag}$ . It has already been noticed that the extinction towards the anticentre direction of the Galaxy is relatively low (cf. Pandey et al. 1989; Joshi 2005). Recent work by Joshi (2005) yields an average value of  $E(B - V) \sim 0.45 \text{ mag}$  which is in agreement with the values ( $E(B - V) = 0.4 - 0.6 \text{ mag}$ ) obtained in the present work.

The reddening of individual stars ( $V_{\text{error}} < 0.1$ ) having spectral type earlier than A0, has been derived using the  $Q$  method (Johnson & Morgan 1953). The distribution of reddening as a function of radial distance is shown in Fig. 9 which indicates a deficiency of reddening material in the central region of the cluster.

The contour maps of reddening in the cluster region are shown in Fig. 10, which indicates that reddening toward the west of the cluster is higher. Individual enhancements of reddening can be seen around some regions including the nebulae Sim 129 and 130 (marked by crosses). The centre of NGC 1893 (marked by asterisk) is less reddened and seems to be devoid of reddening material.

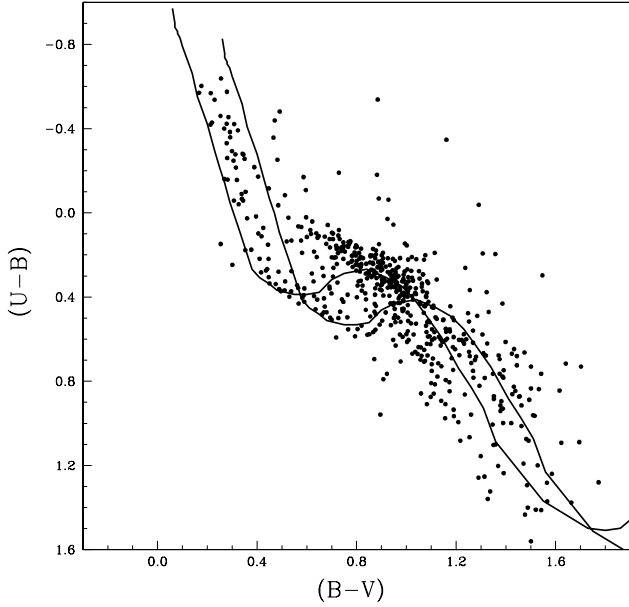


**Figure 8.** The  $(U - B)/(B - V)$  colour-colour diagram for the stars lying within the cluster region ( $r < r_{cl}$ ). The continuous curve represents intrinsic MS by Schmidt-Kaler (1982) shifted along the reddening vector of 0.72 for  $E(B - V)_{min} = 0.4$  and  $E(B - V)_{max} = 0.6$ .

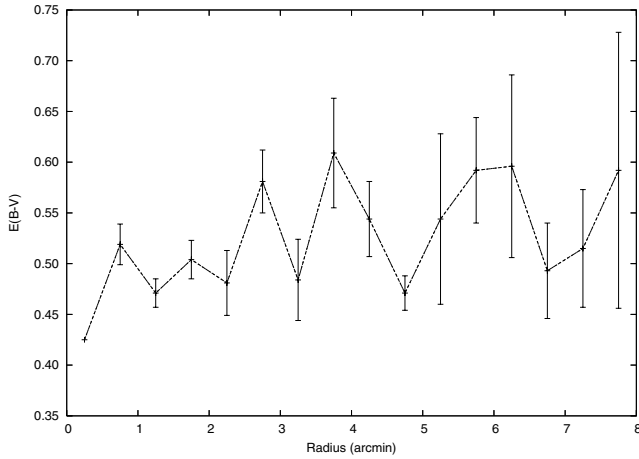


**Figure 9.** Spatial variation of reddening in the cluster region. Error bars represent standard errors.

## 7.2 Reddening law

The interstellar extinction and the ratio of total-to-selective extinction  $R = A_V/E(B - V)$  towards the cluster are important quantities that must be accurately known to determine the distance of the cluster photometrically. To study the nature of the extinction law in the cluster region, we used TCDs as described by Pandey et al. (2003). The TCDs of the form of  $(V - \lambda)$  versus  $(B - V)$ , where  $\lambda$  is one of the wavelengths of the broad-band filters ( $R, I, J, H, K, L$ ) provide an effective method for separating the influence of the normal extinction produced by the diffuse interstellar medium from that of the abnormal extinction arising within regions having a peculiar distribution of dust sizes (cf. Chini & Wargau 1990; Pandey et al. 2000).

The TCDs for the cluster's region ( $r < r_{cl}$ ) are shown in Fig. 11, where NIR data have been taken from the 2MASS. The  $[E(V -$

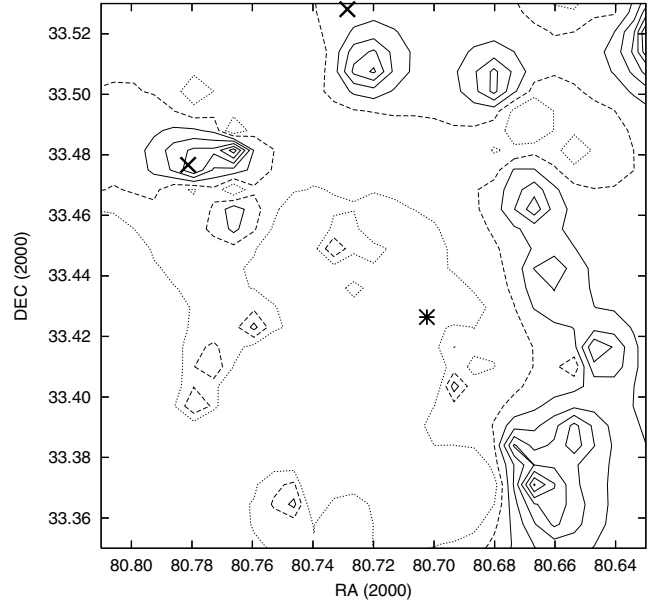


**Figure 10.** Reddening distribution in the cluster region. The dotted, dashed and continuous contours are for  $E(B - V) = 0.51, 0.54$  and  $\geq 0.57$  mag, respectively. The cross and asterisk represent the locations of nebula Sim 129 and cluster centre.

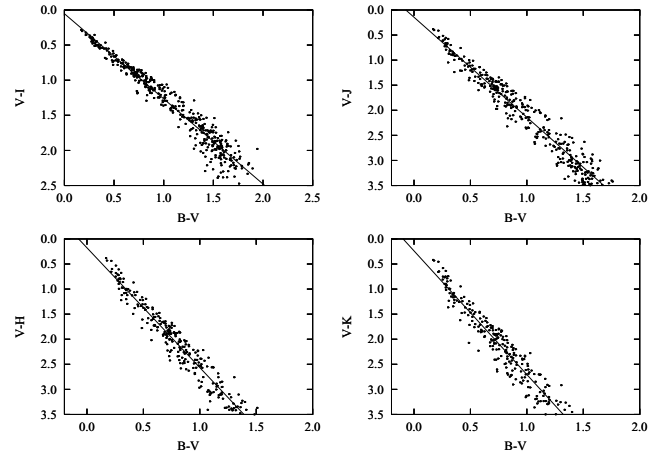


**Figure 11.**  $(V - I), (V - J), (V - H), (V - K)$  versus  $(B - V)$  TCD for stars within cluster region ( $r < r_{cl}$ ). Straight line shows least-square fit to the data.

$\lambda])/[E(B - V)]$  values in the cluster region are estimated as described by Pandey et al. (2003). The slope of the distributions  $m_{cluster}$  (cf. Pandey et al. 2003) is found to be  $1.21 \pm 0.01, 2.00 \pm 0.03, 2.39 \pm 0.04, 2.47 \pm 0.05$  for  $(V - I), (V - J), (V - H), (V - K)$  versus  $(B - V)$  diagrams, respectively. The ratio of total-to-selective extinction in the cluster region,  $R_{cluster}$ , is derived using the procedure given by Pandey et al. (2003). The ratios  $[E(V - \lambda)]/[E(B - V)]$  ( $\lambda \geq \lambda_I$ ) yield  $R_{cluster} = 3.06 \pm 0.07$  which indicates a normal grain size in the cluster region. Tapia et al. (1991) also concluded that the interstellar extinction law in the direction of this cluster appears to be similar to the average Galactic law. Recently, Negueruela et al. (2007) have also supported a normal reddening law in the cluster region.

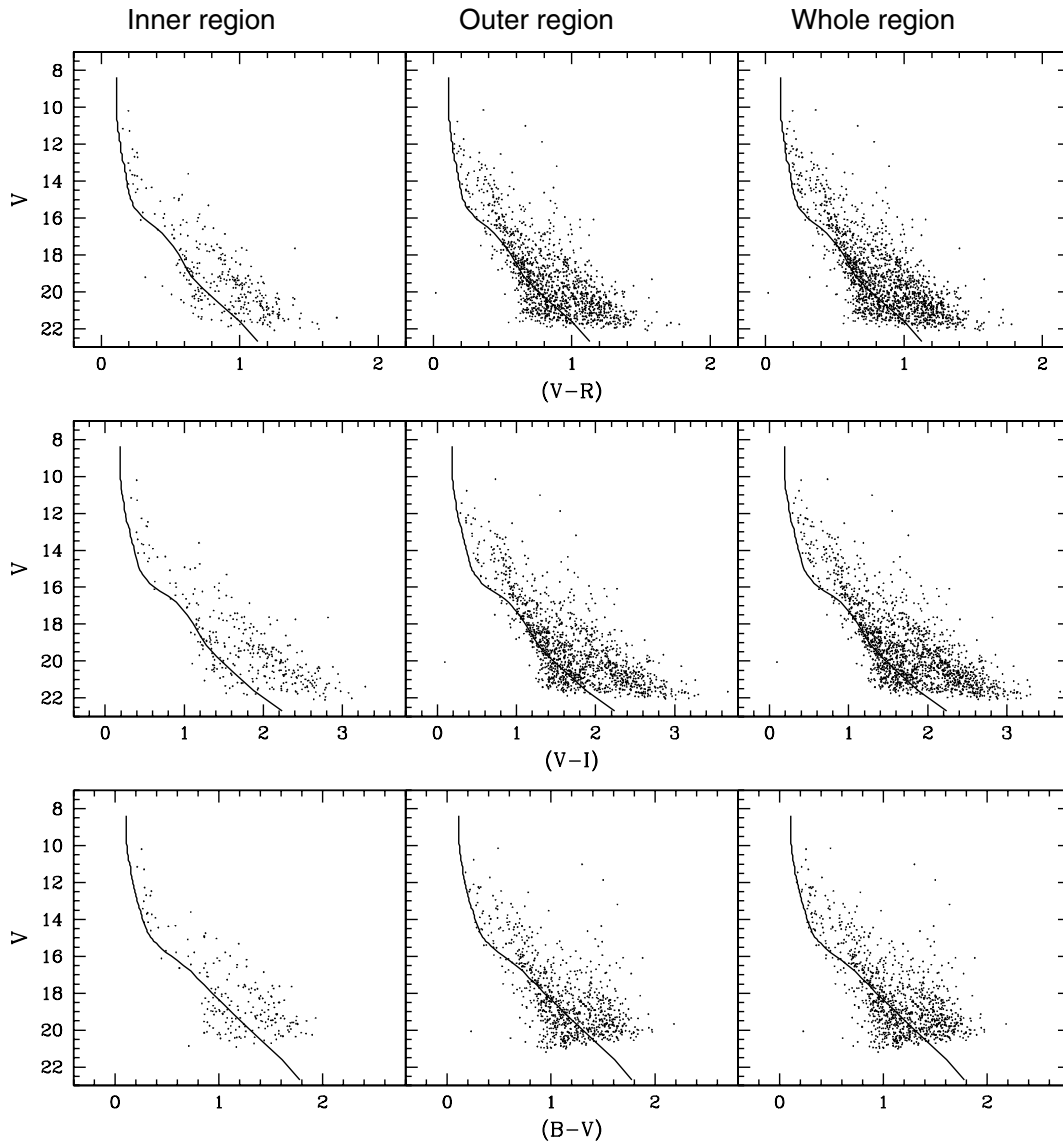


**Figure 12.** The CMDs for stars lying in the two subregions and whole cluster region. The isochrone by Bertelli et al. (1994) for solar metallicity and age = 4 Myr are also plotted for  $E(B - V)_{\min} = 0.4$  and distance modulus of 13.8 mag.

## 8 OPTICAL COLOUR-MAGNITUDE DIAGRAMS

### 8.1 Distance and age of the cluster

CMDs for stars in two subregions and for whole cluster region are shown in Fig. 12. A broad MS, due to variable reddening in the cluster region, extending up to  $V \sim 15$  mag can be noticed in the inner region of the cluster. Distribution of stars fainter than  $V \sim 15$  mag deviates towards red side of MS indicating presence of PMS stars in the cluster region. The effect of field star contamination increases as we move towards outer region of the cluster.

Using  $E(B - V)_{\min} = 0.40$  mag and following relations  $E(U - B)/E(B - V) = 0.72$ ,  $A_V = 3.1 \times E(B - V)$ ,  $E(V - R) = 0.60 \times E(B - V)$ ,  $E(V - I) = 1.25 \times E(B - V)$ , we visually fit theoretical isochrone for log age = 6.6 (4 Myr) and  $Z = 0.02$  by Bertelli et al. (1994) to the blue envelope of the observed MS and found a distance modulus  $(m - M)_V = 13.8 \pm 0.15$  corresponding to a distance of  $3.25 \pm 0.20$  kpc. The reported values of the distance for the cluster

NGC 1893 lie in the range of 3.6 to 4.3 kpc barring the distance (6 kpc) reported by Marco et al. (2001).

### 8.2 Probable members of the cluster

To study the LF/MF, it is necessary to remove field star contamination from the sample of stars in the cluster region. Membership determination is also crucial for assessing the presence of PMS stars, because PMS stars and dwarf foreground stars both occupy similar positions above the zero-age main-sequence (ZAMS) in the CMD. In the absence of proper motion study, we used statistical criterion to estimate the number of probable member stars in the cluster region.

Figs 13(a) and (b) show  $V, (V - I)$  CMDs for the cluster region and field region, respectively. The contamination due to background field population is clearly visible in the cluster region CMD. The background population may belong to Norma-Cygnus (outer) arm (cf. Carraro et al. 2005; Pandey et al. 2006). The thick line on the cluster

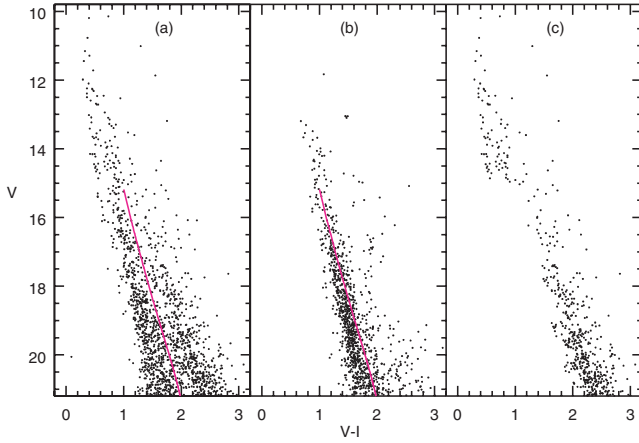


**Figure 13.**  $V/(V - I)$  CMD for (a) stars in the cluster region, (b) stars in the field region and (c) statistically cleaned CMD. Thick line demarcates the contribution background field star contamination.

CMDs demarcates the contamination due to background population. The stars to the left of the line in the cluster CMD are considered as field stars and have not been further considered in the analysis. The cluster CMD shows a significant number of stars towards the right of the line. Majority of these stars should be PMS stars. To remove contamination of field stars from the MS and PMS sample, we statistically subtracted the contribution of field stars from the CMD of the cluster region using the following procedure. For a randomly selected star in the  $V, (V - I)$  CMD of the field region, the nearest star in the cluster's  $V, (V - I)$  CMD within  $V \pm 0.125$  and  $(V - I) \pm 0.065$  of the field star was removed. While removing stars from the cluster CMD, necessary corrections for incompleteness of the data samples were taken into account. The statistically cleaned  $V, (V - I)$  CMD of the cluster region is shown in Fig. 13(c) which clearly shows the presence of PMS stars in the cluster.

Fig. 14 shows statistically cleaned unreddened  $V_0/(V - I)_0$  CMD where stars having spectral type earlier than A0 were individually

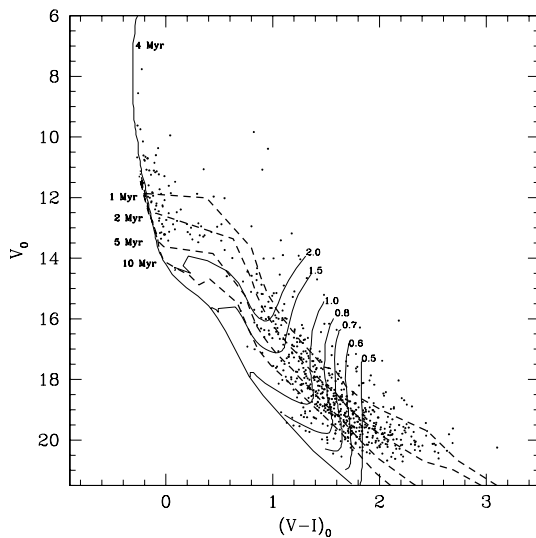


**Figure 14.** Statistically cleaned  $V_0/(V - I)_0$  CMD for stars lying in the cluster region. The isochrone for 4-Myr age by Bertelli et al. (1994) and PMS isochrones of 1, 2, 5, 10 Myr along with evolutionary tracks of different mass stars by Siess et al. (2000) are also shown. All the isochrones are corrected for a distance of 3.25 kpc.

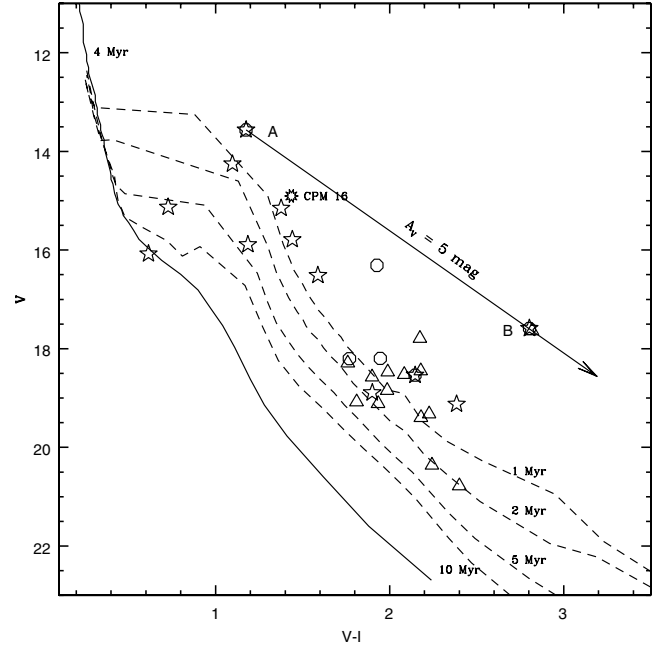


**Figure 15.**  $V, (V - I)$  CMD for  $H\alpha$  emission stars (stars and open circles, cf. Section 9.1) and NIR excess stars (triangles, cf. Section 9.1). Isochrone for 4 Myr by Bertelli et al. (1994, continuous line) and PMS isochrones for 1, 2, 5, 10 Myr by Siess et al. (2000) (dashed lines) are also shown. All the isochrones are corrected for distance of 3.25 kpc and reddening  $E(B - V) = 0.4$ . CPM16 and probable HBe stars (cf. Section 9.1) are also marked by their ID numbers as given in Table 3. The straight line indicates reddening vector for  $A_V = 5$  mag.

unreddened (cf. Section 7.1), whereas mean reddening of the region, estimated from available individual reddening values in that region, was used for other stars. In Fig. 14 we have plotted the isochrone for 4 Myr by Bertelli et al. (1994) and PMS isochrones by Siess, Dufour & Forestini (2000). Evolutionary tracks by Siess et al. (2000) for various masses are also plotted. Fig. 14 manifests that PMS population has an age spread of about 1–5 Myr. To check the reality of the age spread of PMS population, we plotted  $V/(V - I)$  CMD for  $H\alpha$  emission stars and NIR excess stars (see Section 9.1) in Fig. 15, which also indicates an age spread of about 1–5 Myr for the probable PMS stars.

## 9 NEAR-INFRARED COLOUR-COLOUR AND COLOUR-MAGNITUDE DIAGRAMS

NIR observations are very effective for investigating the nature of obscured clusters and the populations of young stellar objects (YSOs) which are embedded in molecular clouds (Lada & Adams 1992).

### 9.1 Colour-colour diagram

In Fig. 16, we have plotted  $(J - H)/(H - K)$  colour-colour diagram for the cluster region ( $r < r_{cl}$ ) and a nearby reference field. The solid and thick dashed curves represent the unreddened MS and giant branch (Bessell & Brett 1988). The parallel dashed lines are the reddening vectors for early- and late-type stars (drawn from the base and tip of the two branches). The dotted line indicates the locus of T Tauri stars (Meyer, Calvet & Hillenbrand 1997). The extinction ratio  $A_J/A_V = 0.265$ ,  $A_H/A_V = 0.155$  and  $A_{K_s}/A_V = 0.090$  have

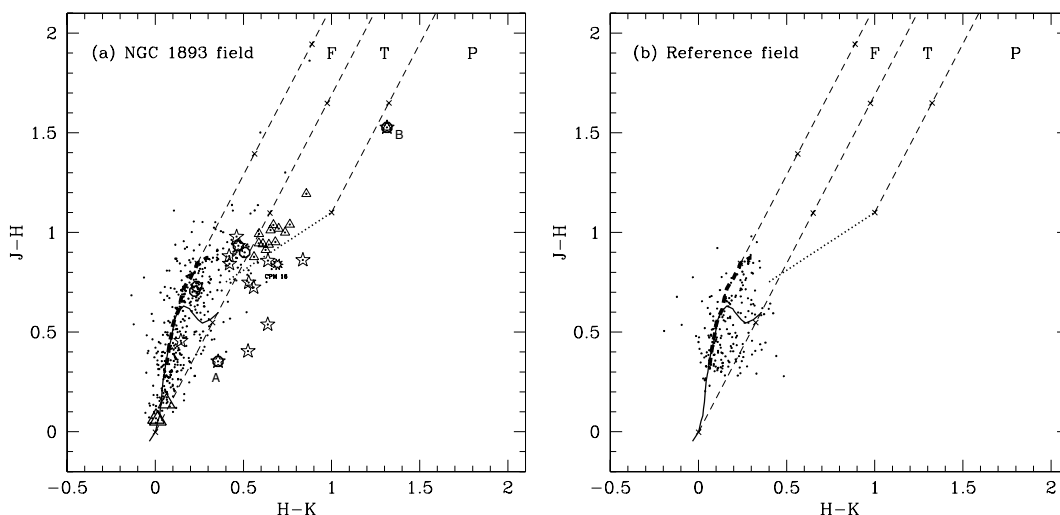


**Figure 16.**  $(J - H)/(H - K)$  colour-colour diagrams of sources detected in the  $JHK_s$  bands with photometric errors less than 0.1 mag in (a) the cluster region ( $r \leq r_c$ ) and (b) the reference field. The sequences for dwarfs (solid curve) and giants (thick dashed curve) are from Bessell & Brett (1988). The dotted line represents the locus of T Tauri stars (Meyer et al. 1997). Dashed straight lines represent the reddening vectors (Cohen et al. 1981). The crosses on the dashed lines are separated by  $A_V = 5$  mag. The star symbols and open circles are the  $H\alpha$  emission stars detected from slitless spectroscopy and narrow band photometry, respectively. Open triangles are probable YSOs (T Tauri stars). Large open triangles are O-type stars. Probable HBe stars and CPM16 are marked.

been taken from Cohen et al. (1981). All the 2MASS magnitudes and colours as well as the curves are in the CIT system. We classified sources into three regions in the colour-colour diagram (cf. Ojha et al. 2004a, and references therein). ‘F’ sources are located between the reddening vectors projected from the intrinsic colour of MS stars and giants and are considered to be field stars (MS stars, giants) or class III/class II sources with small NIR excesses. ‘T’ sources are located redward of region ‘F’ but blueward of the reddening line projected from the red end of the T Tauri locus of Meyer et al. (1997). These sources are considered to be mostly classical T Tauri stars (Class II objects) with large NIR excesses. There may be an overlap in NIR colours of Herbig Ae/Be stars and T Tauri stars in the ‘T’ region (Hillenbrand et al. 1992). ‘P’ sources are those located in the region redward of region ‘T’ and are most likely Class I objects (protostar-like objects; Ojha et al. 2004b). Comparison of Figs 16(a) and (b) shows that the stars in cluster region are distributed in a much wider range as compared to those in reference field. A significant number of sources in the cluster region exhibit NIR excess emission, a characteristic of young stars with circumstellar material. Fig. 16(a) also shows a distribution of  $H\alpha$  emission stars.  $H\alpha$  emission stars detected from slitless spectroscopy (star symbols) are distributed in Herbig Ae/Be region as well as in ‘F’ region, whereas  $H\alpha$  emission stars from narrow-band photometry (open circles) are distributed only in the region ‘F’ of the colour-colour diagram.

The  $H\alpha$  emission star B (Table 3) is relatively more obscured and shows a large NIR excess. This star lies near to  $H\alpha$  emission star A, which has been assigned as an HBe star (S3R1N3) by Marco & Negueruela (2002). The  $V, (V - I)$  CMD (Fig. 15) indicates that the star B is more obscured by  $\sim 4.0$  mag in comparison to star A. A correction of  $A_V \sim 4.0$  mag puts star B in the HAeBe region in Fig. 16.

## 9.2 Colour-magnitude diagram

The CMDs are useful tool for studying the nature of the stellar population within star-forming regions. In Fig. 17(a), we have plotted

$J/(J - H)$  CMD for the stars within cluster region. Using the relation  $A_J/A_V = 0.265$ ,  $A_{J-H}/A_V = 0.110$  (Cohen et al. 1981) and  $A_V = 3.1 \times E(B - V)$ , the isochrones for age 4 Myr and PMS isochrones for ages 1 and 10 Myr by Bertelli et al. (1994) and Siess et al. (2000), respectively, have been plotted assuming the distance of 3.25 kpc and extinction  $E(B - V)_{\min} = 0.4$  as obtained from the optical data. Probable YSOs (T Tauri-type stars) obtained from the colour-colour diagram and  $H\alpha$  emission stars are shown by open triangles and star symbols/open circles, respectively. Most of the probable T Tauri and  $H\alpha$  emission stars have age  $\leq 1$  Myr. Fig. 17(b) shows  $K/(H - K)$  CMD for the stars lying within the cluster region. The symbols are the same as in Fig. 16. The nearly vertical lines represent the ZAMS at a distance of 3.25 kpc reddened by  $A_V = 0, 1.24$  and 15 mag, respectively. The intrinsic colours are taken from Koorneef (1983). The parallel slanted lines trace the reddening zones for each spectral type.

Fig. 18 represents  $J/(J - H)$  diagram for probable YSO candidates identified in Fig. 16. The symbols are same as in Fig. 16. The mass of the probable YSO candidates can be estimated by comparing their location on the CMD with the evolutionary models of PMS stars. The solid curve, taken from Siess et al. (2000) denotes the locus of 1-Myr-old PMS stars having masses in the range of 0.1 to 3.5  $M_\odot$ . To estimate the stellar masses, the  $J$  luminosity is recommended rather than that of  $H$  or  $K$ , as the  $J$  band is less affected by the emission from circumstellar material (Bertout, Basri & Bouvier 1988). The majority of the YSOs have masses in the range 3.0 to 1.0  $M_\odot$  indicating that these may be T Tauri stars. A few stars having mass greater than 3.0  $M_\odot$  may be candidates for Herbig Ae/Be stars.

## 10 INITIAL MASS FUNCTION

The distribution of stellar masses that form in a star formation event in a given volume of space is called IMF and together with star formation rate, the IMF dictates the evolution and fate of galaxies and star clusters (Kroupa 2002).

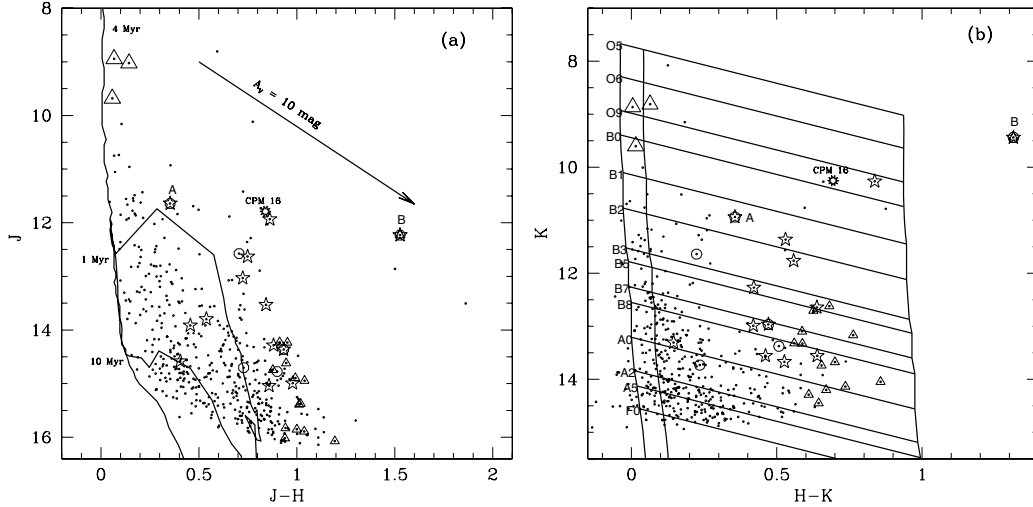


**Figure 17.** (a)  $J/(J - H)$  CMD of the stars within cluster region ( $r \leq r_{cl}$ ). The symbols are same as in Fig. 16. The isochrone of 4 Myr ( $Z = 0.02$ ) by Bertelli et al. (1994) and PMS isochrones of age 1 and 10 Myr taken from Siess et al. (2000) corrected for a distance of 3.25 kpc, and reddening  $E(B - V)_{min} = 0.40$  are also shown. (b)  $K/(H - K)$  CM diagram for the stars within cluster region ( $r \leq r_{cl}$ ). The symbols are same as in Fig. 16. The vertical solid lines from left to right indicate the MS track at 3.25 kpc reddened by  $A_V = 0, 1.24, 15$  mag, respectively. The intrinsic colours are taken from Koornneef (1983). Slanting horizontal lines identify the reddening vectors for each spectral type marked in the figure. Probable HBe stars and CPM16 are marked.

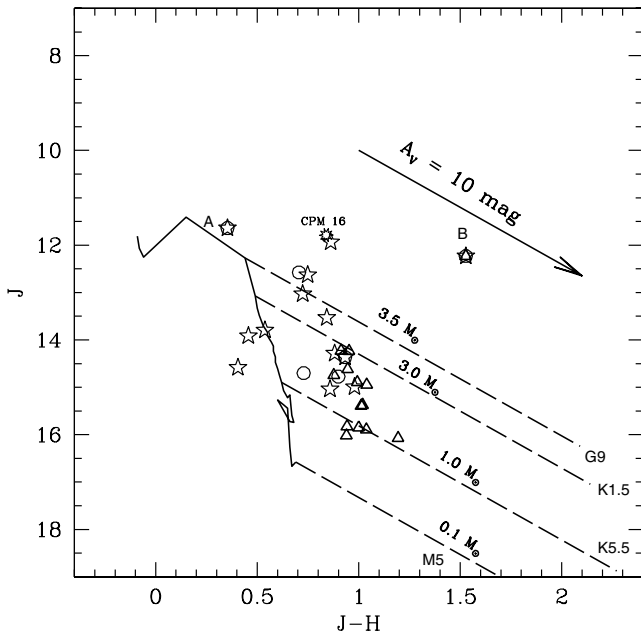


**Figure 18.**  $J/(J - H)$  CMD for the YSO candidates in cluster region ( $r \leq r_{cl}$ ). The symbols are same as in Fig. 15. The solid curve denotes PMS isochrone of 1 Myr, derived from Siess et al. (2000), corrected for a distance of 3.25 kpc. Masses range from 3.5 to 0.1  $M_{\odot}$  from top to bottom. The dashed oblique reddening lines denote the positions of PMS stars of 0.1, 1, 3.0 and 3.5  $M_{\odot}$ .

The MF is often expressed by the power law,  $N(\log m) \propto m^{\Gamma}$  and the slope of the MF is given as

$$\Gamma = d \log N(\log m) / d \log m,$$

where  $N(\log m)$  is the number of star per unit logarithmic mass interval. In the solar neighbourhood the classical value derived by Salpeter (1955) is  $\Gamma = -1.35$ .

With the help of statistically cleaned CMD, shown in Fig. 14, we can derive the MF using the theoretical evolutionary model of Bertelli et al. (1994). Since post-MS age of the cluster is  $\sim 4$  Myr, the stars having  $V < 15$  mag ( $V_0 < 13.5$ ;  $M > 2.5 M_{\odot}$ ) have been considered to be on the MS. For the MS stars, the LF was converted to the MF using the theoretical model by Bertelli et al. (1994) (cf. Pandey et al. 2000, 2001). The MF for PMS stars was obtained by counting the number of stars in various mass bins (shown as evolutionary tracks) in Fig. 14. The MF in two subregions as well as for the whole cluster is given in Table 7 and plotted in Fig. 19.

Table 8 indicates that the slopes of the MF of MS and of PMS stars in the inner region of the cluster are almost the same and can be represented by  $\Gamma = -1.19 \pm 0.03$  which is slightly shallower than the Salpeter value. This indicates that there is no mass segregation in the inner region of the cluster. In the outer region as well as for the whole cluster region, the  $\Gamma$  for PMS stars seems to be shallower than the  $\Gamma$  for the MS stars indicating a break in the slope of the MF at  $\sim 2 M_{\odot}$ . However, a single slope for the MF, in the outer region and whole cluster, can also be fitted to the entire observed

**Table 7.** The MF of the NGC 1893 cluster. The number of probable cluster members ( $N$ ) has been obtained after subtracting the expected contribution of field stars.  $\log \phi$  represents  $\log(N/d \log m)$ .

Mass ( $M/M_{\odot}$ )	Mean $\log M/M_{\odot}$	Inner region $N$	Outer region $N$	Whole region $N$
17.7–12.3	1.1759	1	1	2
12.3–8.4	1.0147	2	3	5
8.4–5.6	0.8451	4	10	14
5.6–3.7	0.6650	6	16	22
3.7–2.5	0.4868	8	25	33
2.0–1.5	0.2432	13	37	50
1.5–1.0	0.0969	24	57	81
1.0–0.8	-0.0459	20	46	66
0.8–0.7	-0.1249	17	31	48
0.7–0.6	-0.1872	20	40	60

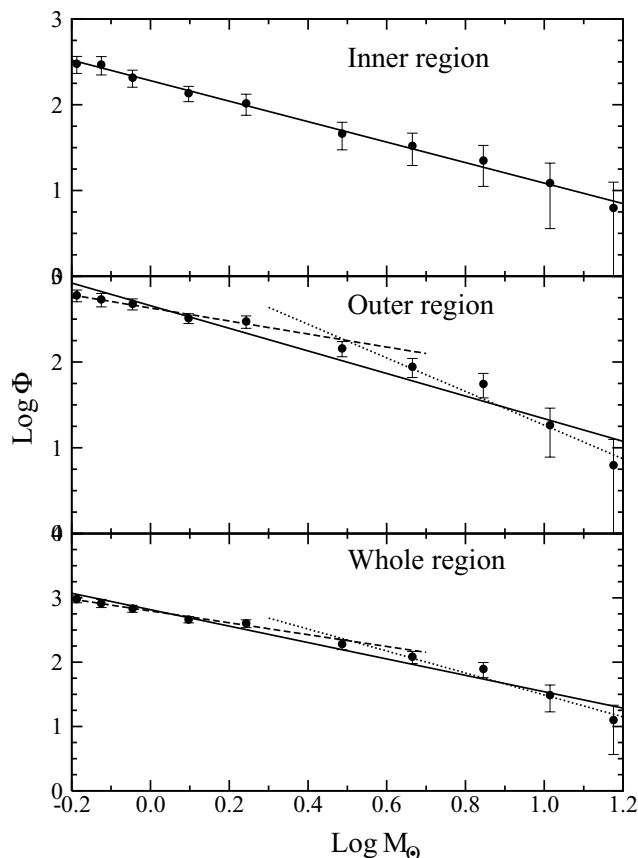


**Figure 19.** A plot of the MF in the cluster.  $\log \phi$  represents  $\log(N/d \log m)$ . The error bars represent  $\pm \sqrt{N}$  errors. The solid line shows a least-square fit to the entire mass range  $0.6 < M/M_{\odot} < 17.7$ .

**Table 8.** MF ‘ $\Gamma$ ’.

Region	‘ $\Gamma$ ’ (MS)	‘ $\Gamma$ ’ (PMS)	‘ $\Gamma$ ’ (MS+PMS)
Inner	$-1.25 \pm 0.13^a$	$-1.15 \pm 0.11^b$	$-1.19 \pm 0.03^c$
Outer	$-1.96 \pm 0.26^a$	$-0.76 \pm 0.09^b$	$-1.32 \pm 0.12^c$
Whole	$-1.71 \pm 0.20^a$	$-0.88 \pm 0.09^b$	$-1.27 \pm 0.08^c$

<sup>a</sup>Mass range ( $2.5 < M/M_{\odot} < 17.7$ ).

<sup>b</sup>Mass range ( $0.6 < M/M_{\odot} < 2.0$ ).

<sup>c</sup>Mass range ( $0.6 < M/M_{\odot} < 17.7$ ).

mass range ( $0.6 < M/M_{\odot} < 17.7$ ) with  $\Gamma = -1.32 \pm 0.12$  and  $-1.27 \pm 0.08$ , respectively.

Effect of mass segregation can be seen on the MS stars. The  $\Gamma$  for the MS stars is steeper in the outer region indicating a preferential distribution of relatively massive stars towards the cluster centre, whereas  $\Gamma$  for the PMS stars is steeper in the inner region as compared to the  $\Gamma$  in the outer region. However, the difference in the slopes is rather small ( $2.5\sigma$  and  $2.7\sigma$  in the case of MS and PMS stars, respectively).

For the mass range  $2.5 \leq M/M_{\odot} \leq 17.7$ , the MF for the whole cluster region ( $r \leq 6$  arcmin) can be represented by  $\Gamma = -1.71 \pm 0.20$  which is in agreement with the value ( $\Gamma = -1.6 \pm 0.3$ ) given by Massey et al. (1995b).

## 11 K-BAND LUMINOSITY FUNCTION

In order to obtain the  $K$ -band luminosity function (KLF) of the cluster, it is essential to take into account the incompleteness of the data as well as the foreground and background source contaminations. The completeness of the data is estimated using the ADDSTAR routine of DAOPHOT as described in Section 5. To take into account foreground/background field star contamination we used both the Besançon Galactic model of stellar population synthesis (Robin et al. 2003) and the nearby reference field stars. Star counts are predicted using the Besançon model in the direction of the control field. We checked the validity of the simulated model by comparing the model KLF with that of the control field (see Fig. 20a) and found that both the KLFs match rather well. An advantage of using the model is that we can separate the foreground ( $d < 3.25$  kpc) and background ( $d > 3.25$  kpc) field stars. As mentioned in Section 7.1, the foreground extinction using optical data was found to be  $A_V \sim 1.24$  mag. The model simulations with  $A_V = 1.24$  mag and  $d < 3.25$  kpc gives the foreground contamination.

The background population ( $d > 3.25$  kpc) was simulated with  $A_V = 1.86$  mag in the model. We thus determined the fraction of the

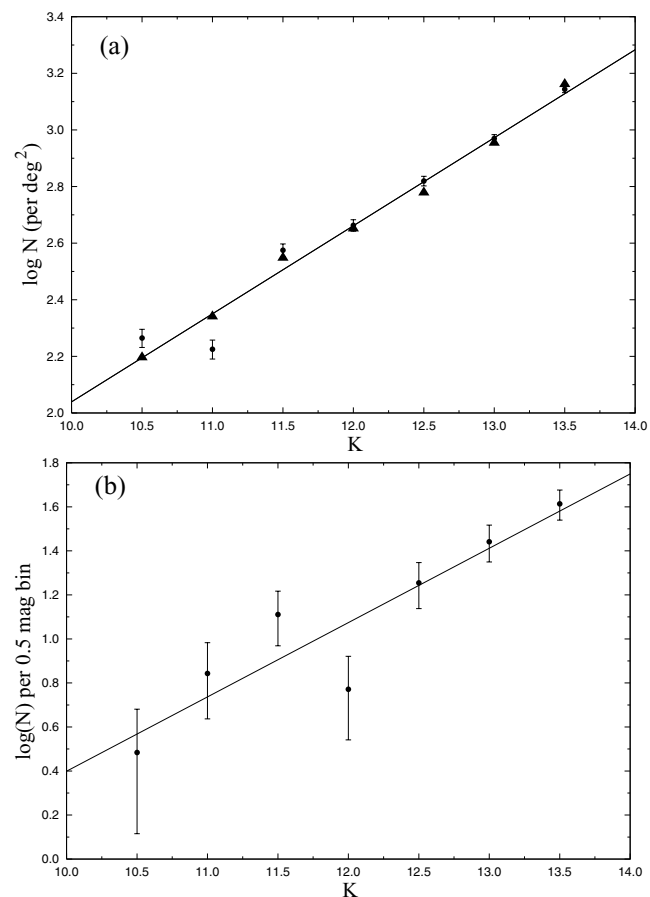


**Figure 20.** (a) Comparison of the observed KLF in the reference field and the simulated KLF from star count modelling. The filled circles denote the observed  $K$ -band star counts in the reference field, and triangles represent the simulation from the Galactic model (see the text). The star counts are number of star per  $\text{deg}^2$  and the error bars represents  $\pm \sqrt{N}$  errors. The KLF slope ( $\alpha$ , see Section 11) of the reference field (solid line) is  $0.31 \pm 0.03$ . The simulated model is also giving the same value of slope ( $0.31 \pm 0.01$ ). (b) The corrected KLF for the probable members in the cluster. The straight line is the least-square fit to the data points in the range 10.5–13.5 mag.

contaminating stars (foreground+background) over the total model counts. This fraction was used to scale the nearby reference field and subsequently the star counts of the modified control field were subtracted from the KLF of the cluster to obtain the final corrected KLF. The KLF is expressed by the following power law:

$$\frac{dN(K)}{dK} \propto 10^{\alpha K},$$

where  $[dN(K)]/(dK)$  is the number of stars per 0.5 mag bin and  $\alpha$  is the slope of the power law. Fig. 20(b) shows the KLF for the cluster region which indicates a slope of  $\alpha = 0.34 \pm 0.07$ . The slope is consistent with the average value of slopes ( $\alpha \sim 0.4$ ) for young clusters (Lada et al. 1991; Lada & Lada 1995, 2003).

## 12 MASS SEGREGATION

There are evidences for mass segregation in a few Galactic as well as Large Magellanic Cloud (LMC) star clusters, with the highest mass stars preferentially found towards the centre of the cluster (see e.g. Sagar et al. 1988; Sagar & Richtler 1991; Pandey, Mahra & Sagar 1992; Fischer et al. 1998; Pandey et al. 2001, 2005). Although, as per standard theory where stars in clusters evolve rapidly towards a state of energy equipartition through stellar encounters, consequently mass segregation – in the sense that more massive stars tend to lie near the centre – is well accepted. However, observations of mass segregation in very young clusters (e.g. Pandey et al. 1992; Hillenbrand 1997) suggest that in the case of a few young clusters the mass segregation may be the imprint of star formation process itself (Pandey et al. 2005).

To characterize the degree of mass segregation in NGC 1893 we subdivided the MS sample into two mass groups ( $5.6 < M/M_{\odot} \leq 17.7$ ,  $2.5 < M/M_{\odot} \leq 5.6$ ). Fig. 21 shows cumulative distribution of MS stars as a function of radius in two different mass groups. The figure indicates an effect of mass segregation in the cumulative distribution in the sense that more massive stars ( $5.6 < M/M_{\odot} \leq 17.7$ ) tend to lie toward the cluster centre. The Kolmogorov–Smirnov test confirms the statement that the cumulative distribution of massive stars in the cluster is different from the cumulative distribution of relatively less massive stars at a confidence level of 99 per cent. Because of the dynamical relaxation, low-mass stars in a cluster may acquire larger random velocities, consequently occupy a larger volume than high-mass stars (cf. Mathieu 1985; McNamara & Sekiguchi 1986; Mathieu & Latham 1986). We estimated the relaxation time to decide whether the mass segregation discussed

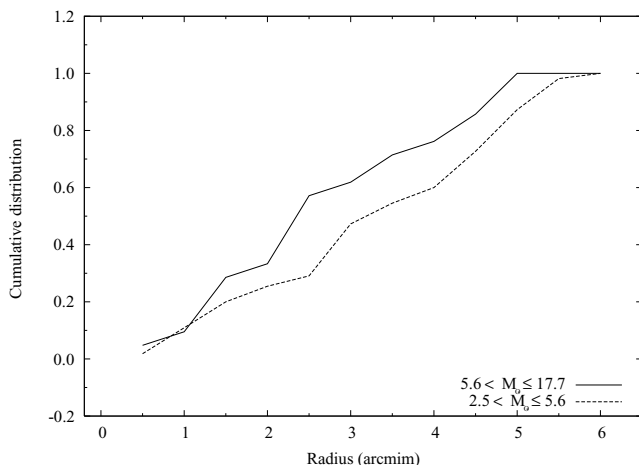


**Figure 21.** Cumulative radial distribution of MS stars in two mass intervals.

**Table 9.** Parameters of the cluster.

Mass range	Total mass ( $M_{\odot}$ )	No. of stars	Average mass $\bar{m}(M_{\odot})$	$T_E$ (Myr)
$2.5 < M/M_{\odot} < 17.7$	$\sim 374$	$\sim 78$	$\sim 4.8$	$\sim 12$
$0.6 < M/M_{\odot} < 2.0$	$\sim 333$	$\sim 315$	$\sim 1.1$	$\sim 35$
$0.6 < M/M_{\odot} < 17.7$	$\sim 710$	$\sim 390$	$\sim 1.8$	$\sim 29$

above is primordial or due to dynamical relaxation. To estimate the dynamical relaxation time  $T_E$ , we used the relation

$$T_E = \frac{8.9 \times 10^5 N^{1/2} R_h^{3/2}}{\bar{m}^{1/2} \log(0.4N)},$$

where  $N$  is the number of cluster stars,  $R_h$  is the radius containing half of the cluster mass and  $\bar{m}$  is the average mass of cluster stars (Spitzer & Hart 1971). The total number of MS stars and the total mass of the MS stars in the given mass range ( $2.5 \leq M/M_{\odot} \leq 17.7$ ) is obtained with the help of LF/MF. This mass should be considered as the lower limit of the total mass of the cluster. For the half-mass radius we used half of the cluster extent, i.e. 2.85 pc. Various parameters used to estimate  $T_E$  for the cluster are given in Table 9. Using these numbers, the estimated relaxation time  $T_E$  comes out to be larger than the age of the cluster. This indicates that the observed mass segregation of MS stars in the cluster should be of largely primordial nature.

## 13 SPATIAL DISTRIBUTION: GLOBAL OVERVIEW OF STAR FORMATION AROUND THE CLUSTER

Massive O-type stars may have strong influence and significantly affect the entire star-forming regions. On one hand, energetic stellar winds from massive stars could evaporate nearby clouds and consequently terminate nearby star formation by destroying the gas clouds. Alternatively, stellar winds and shock waves from supernova explosion may squeeze molecular clouds and induce subsequent star formation. Could both of these effects occur in different parts of the same star-forming regions? Herbig (1962) suggested that low- and intermediate-mass stars form first and with the formation of the most massive star in the regions, the cloud gets disrupted and star formation ceases. Alternatively, Elmegreen & Lada (1977) propose the low-mass stars form first throughout the entire molecular cloud. After formation of massive stars, the expanding ionization fronts play a constructive role to incite a sequence of star formation activities in the neighbourhood. The morphological details of the environment around NGC 1893 containing several O-type stars can be used to probe the different stages of evolution of star formation present in this cloud complex.

In Fig. 22 spatial distribution of O-type stars, IR-excess sources (probable T Tauri-type stars) and  $H\alpha$  stars have been displayed on a  $40 \times 40$  arcmin<sup>2</sup> DSS-2 (Digital Sky Survey-2)  $R$ -band image around the cluster. Most of the YSOs seem to align toward from north-east to south-west. The apparent concentration of the YSOs can be seen around the nebulous region Sim 129. The distribution of YSOs indicates that star formation in the cluster might have taken place along the direction of Sim 129. Similar conclusion has also been reported by Negueruela et al. (2007). To study whether stars show any sequence in age we selected three subregions having equal area and a field region outside the cluster region, as shown in Fig. 22. Figs 23(a) and (b) show unreddened  $V/(V-I)$  CMDs for the

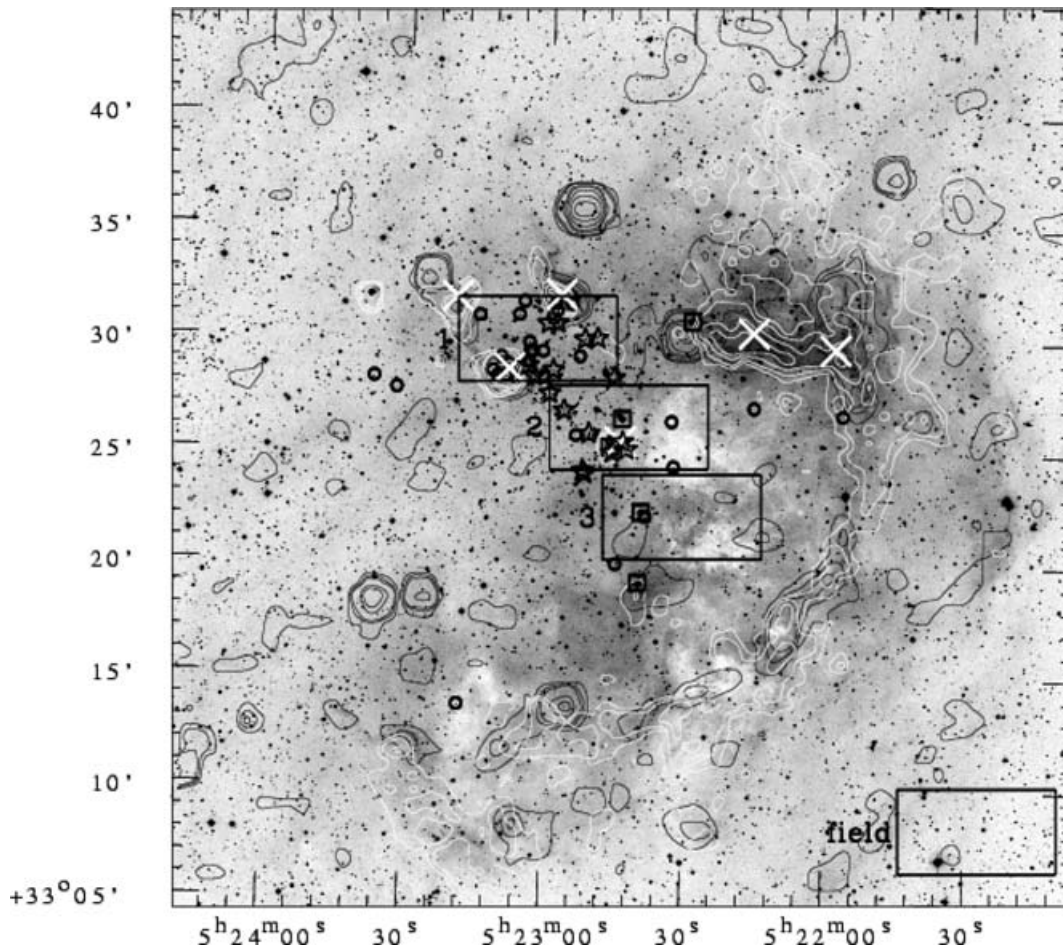


**Figure 22.** Spatial distributions of O-type stars (open square box), IR-excess sources (probable T Tauri-type stars, open circles),  $H\alpha$  (star symbols) stars and *IRAS* points sources (crosses) are overlaid on DSS-2 *R*-band image. NVSS (1.4 GHz) radio contours (black contours) and MSX *A*-band intensity contours (white contours) has also been shown. The MSX *A*-band contours are 2.5, 3, 4, 5, 10, 20, 40, 60, 80 per cent of the peak value  $3.25 \times 10^{-5} \text{ W m}^{-2} \text{ sr}^{-1}$  and the NVSS radio contours are 0.2, 0.5, 1, 3, 5, 10, 20, 40, 60, 80 per cent of the peak value  $0.45 \text{ Jy beam}^{-1}$ . The abscissa and the ordinates are for the J2000.0 epoch. Three subregions and a field region are also marked.

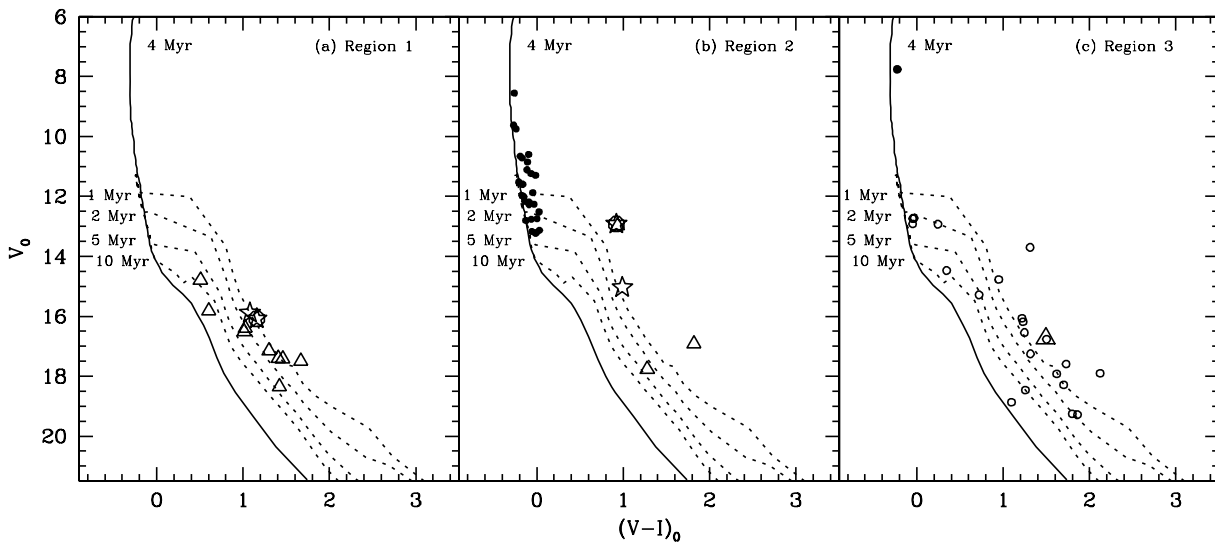


**Figure 23.**  $V_0/(V-I)_0$  CMDs for the probable YSOs in the three different regions. The triangle and star symbol represent NIR excess and  $H\alpha$  stars, respectively. Probable MS stars in the region 2 are shown by filled circles. Stars around O-type star in region 3 are shown by open circles.

**Table 10.** Statistics of the YSOs in the three different regions. Numbers given in parenthesis are in percentage.

Region	Totals stars	NIR excess stars	H $\alpha$ stars (slitless)	All YSOs
1	139	16 (21)	8+7 (20) <sup>a</sup>	29 (38) <sup>b</sup>
2	145	5 (6)	6+2 (10) <sup>a</sup>	12 (15) <sup>c</sup>
3	99	1 (3)	0	1 (3)
Field	63			

<sup>a</sup>H $\alpha$  stars taken from Negueruela et al. (2007).

<sup>b</sup>Two H $\alpha$  stars have NIR excess.

<sup>c</sup>One H $\alpha$  stars has NIR excess.

probable YSOs (triangles, NIR excess stars; star symbols, H $\alpha$  stars) in regions 1 and 2, respectively. In region 2 CMD we have also plotted probable MS stars. The  $(J - H)/(H - K)$  TCD was used to estimate  $A_V$  for each YSO by tracing back to the intrinsic line of Meyer et al. (1997) along the reddening vector. Probable MS stars are dereddened individually as described in Section 7.1. In region 3 (Fig. 23c) only one NIR excess star was found. There seems to be a small clustering around O-type star in the region 3. Stars within a 1 arcmin of the O-type stars are also plotted in Fig. 23(c). These stars were unreddened using the  $E(B - V)$  value of the O-type star. Fig. 23 manifests that the YSOs lying near the nebula Sim 129 have age  $\sim 1-2$  Myr. The post-MS age of the cluster stars is  $\sim 4$  Myr, whereas the YSOs near the cluster region have age  $< 1-2$  Myr. The probable PMS stars in the region 3 have age 1–5 Myr, whereas O-type star has an age  $\sim 4$  Myr. To further verify the age sequence we estimate the percentage of YSOs in these three regions. The statistics is given in Table 10. H $\alpha$  photometry for the nebula Sim 129 region was not carried out therefore H $\alpha$  photometry is not used for the statistics. Table 10 indicates a significant excess of YSOs in the region 1 (38 per cent) in comparison to the region 2 (15 per cent) and region 3 (3 per cent). The distribution of YSOs further supports a small-scale sequential star formation. The O7–8 star (HD 242935) at the centre of the cluster might have triggered the star formation towards the direction of nebula Sim 129.

Using the  $^{12}\text{CO}$  survey Leisawitz, Bash & Thaddeus (1989) concluded that a molecular cloud (NGC 1893A) is associated with the cluster. The peak of the  $^{12}\text{CO}$  contours is located at the south-west of the cluster centre. The cloud NGC 1893A is in front of the cluster and it may be receding from the cluster (Leisawitz et al. 1989). The differential extinction towards the cluster is  $\sim 0.2$  mag indicating that the cloud contains low-density gas. In Fig. 22 NVSS (1.4 GHz) radio cont. emission contour maps (black contours) and MSX A-band IR contour maps (white contours) are also overlaid. The location of *IRAS* point sources has been represented by crosses. The gross morphologies of the radio contour map and MSX A-band contour map are similar, though the emission from the MSX A band is much more extended. The majority of emission from radio as well as MSX A band comes from an arc-shaped region embracing the cluster from north-west to south-east. To the north-west of the cluster, the contours show relatively steep intensity gradient towards the cluster. This region also harbours two *IRAS* sources.

The MSX A-band intensity map indicates presence of several discrete sources (including Sim 129 and 130) representing high-density clumps and region of further star formation. It is interesting to point out that five H $\alpha$ , two NIR excess stars (see Fig. 22) and two PMS stars from Marco & Negueruela (2002) lie on the rim of the cloud towards west of the cluster. This indicates, as suggested

by Marco & Negueruela (2002), this region is in the process of emerging from the parental cloud.

Fig. 24 shows the *IRAS*-HIRES intensity maps for the cluster region at 12  $\mu\text{m}$  (top left), 25  $\mu\text{m}$  (top right), 60  $\mu\text{m}$  (bottom left) and 100  $\mu\text{m}$  (bottom right). The contour maps also show a bright arc-shaped rim on the western side of the cluster, as seen in MSX as well as NVSS radio contour maps. Such a morphology implies that the H II region is ionization bounded towards the western side of the cluster.

The cluster region shows emission in MIR (MSX A band and *IRAS* 12  $\mu\text{m}$ ) indicating presence of warm dust in the region but no radio emission. The nebula Sim 129 is associated with the ionized region and also shows emission in MIR and far-infrared (FIR) (*IRAS* 12–100  $\mu\text{m}$ ), whereas the nebula Sim 130 does not show significant emission in FIR (60 and 100  $\mu\text{m}$ ). The clump to the north-west of the cluster (hereafter clump A,  $\alpha_{2000} = 05^{\text{h}}22^{\text{m}}2$ ,  $\delta_{2000} = 33^{\circ}33'$ ), which harbours two *IRAS* sources, shows presence of ionized gas along with warm dust (MSX A band, *IRAS* 12 and 25  $\mu\text{m}$ ) as well as cold dust (*IRAS* 60–100  $\mu\text{m}$ ). This clump also shows H $\alpha$  emission (see Fig. 25). The above-mentioned features indicate ongoing star formation activity in the clump. There is another clump towards south of the cluster (clump B,  $\alpha_{2000} = 05^{\text{h}}22^{\text{m}}6$ ,  $\delta_{2000} = 33^{\circ}18'5$ ) which shows strong emission in FIR (60 – 100  $\mu\text{m}$ ). This clump also shows emission in H $\alpha$  and an O7-type star is located in the clump B.

Distribution of YSOs and intensity maps of radio, NIR and FIR emissions in NGC 1893 region indicate four major clumps/condensations including Sim 129 and 130. YSOs distributed around Sim 129 and 130 are found to have ages  $\sim 1-3$  Myr. The angular distance of Sim 129 and 130 from the cluster is about  $\sim 5.6$  and  $\sim 6.1$  arcmin, respectively. Clump A (angular distance  $\sim 10$  arcmin) shows signature of ongoing star formation. A few NIR excess stars are visible towards the direction of the clump. As we have mentioned above, the region towards the clump A seems to be in process of emerging out from the parental cloud, so many more YSOs may still be embedded in the cloud.

The contribution of UIBs due to polycyclic aromatic hydrocarbons (PAHs) to the MIR emissions in the four MSX bands has been studied using the scheme developed by Ghosh & Ojha (2002). The emission from each pixel is assumed to be a combination of two components, namely the thermal cont. from dust grains (grey body) and the emission from the UIB features in the MSX bands. The scheme assumes a dust emissivity of the power law form  $\epsilon_{\lambda} \propto \lambda^{-1}$  and the total radiance due to the UIBs in band *C* is proportional to that in band *A*. A self-consistent non-linear chi-square minimization technique is used to estimate the total emission from the UIBs, the dust temperature and the optical depth. The spatial distribution of the UIB emission, temperature map and optical depth ( $\tau_{10}$  at 10  $\mu\text{m}$ ) contour map with an angular resolution of  $\sim 18$  arcsec (for the MSX survey) extracted for the cluster region is shown in Fig. 25. Morphologically all are similar with the intensity peaks matching rather well with each other. This indicates the presence of high densities near the embedded sources.

We have used the *IRAS*-HIRES maps at 12 and 25  $\mu\text{m}$  to generate the spatial distribution of dust colour temperature  $T(12/25)$  and optical depth at 25  $\mu\text{m}$  ( $\tau_{25}$ ) (cf. Ghosh et al. 1993). An emissivity law of  $\epsilon_{\lambda} \propto \lambda^{-1}$  was assumed to generate these maps. The dust colour temperature and optical depth maps representing warmer dust component are presented in Fig. 26. The latter is shown in Fig. 26 (left), which is scaled to 10  $\mu\text{m}$  by a  $\lambda^{-1}$  emissivity law to compare with the MSX  $\tau_{10}$  map. The distribution is centrally dense with optical depth peak and lower temperature at the centre. The region is

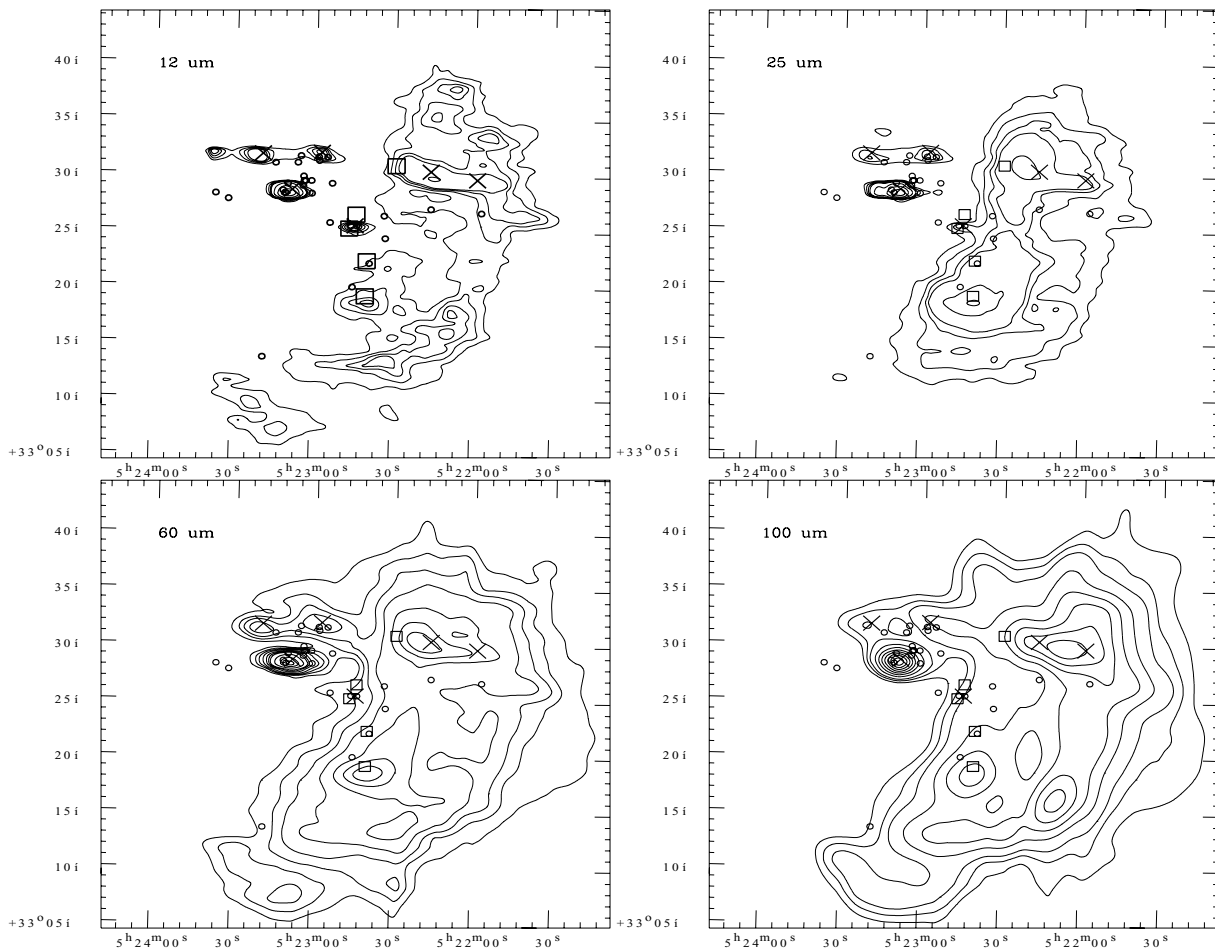


**Figure 24.** The *IRAS*-HIRES intensity maps at 12  $\mu\text{m}$  (top left), 25  $\mu\text{m}$  (top right), 60  $\mu\text{m}$  (bottom left) and 100  $\mu\text{m}$  (bottom right). The contours are at 2, 3, 4, 5, 10, 20, 40, 60, 80 per cent of the peak value of 150 and 460  $\text{MJy sr}^{-1}$  at 12 and 25  $\mu\text{m}$ , respectively; 3, 5, 7, 10, 15, 20, 25, 40, 60, 80 per cent of the peak value of 990  $\text{MJy sr}^{-1}$  at 60  $\mu\text{m}$  and 10, 15, 20, 30, 40, 50, 60, 70, 80, 90 per cent of the peak value of 426  $\text{MJy sr}^{-1}$  at 100  $\mu\text{m}$ . The symbols are as same as in Fig. 22.

showing cometary appearance. Such a morphology can result if a massive star(s) is(are) formed away from the centre of a molecular cloud. This will cause the H II region to expand into an asymmetric density distribution and so becomes cometary (Israel 1978). From the orientation of the two emission nebulae and the arc-shaped ring around the cluster centre it is suggested that the central O-type star(s) is(are) most likely responsible for the cometary morphology and the trigger of star formation.

A comparison is also made between the  $\tau_{10}$  maps generated from the higher angular resolution MSX maps (Fig. 25, bottom left) and that based on the *IRAS*-HIRES maps at 12 and 25  $\mu\text{m}$  (Fig. 26, left). The MSX  $\tau_{10}$  map is brought to the same angular resolution as of HIRES for the comparison. The peak optical depth is  $8.54 \times 10^{-5}$  for the map based on MSX. The corresponding value from the *IRAS*-HIRES map is  $1.36 \times 10^{-5}$ . These derived values are in reasonable agreement considering that they are based on instruments with very different angular resolutions. The difference in the peak values of  $\tau_{10}$  may be a result of the following effects: beam dilution, clumpy interstellar medium and the contribution of UIB emission. In particular in our study the contribution of the UIBs emission has been removed in generating the optical depth in the modelling of the MIR emission from the MSX bands, however, the *IRAS*-HIRES maps represent the emission from dust and UIB carriers [e.g. the

emission from the UIB features falls within the *IRAS* 12- $\mu\text{m}$  band ( $\sim 8\text{--}15 \mu\text{m}$ )].

The distribution of reddening (cf. Section 7.1) and close inspection of Fig. 22 indicates the presence of a region of low density of reddening material at the centre of the cluster. Similar trend has been noticed in a few H II regions (e.g. 30 Dor, Brandl et al. 1996 and NGC 3603, Pandey et al. 2000). A reasonable explanation for this lack of gas and dust in the central region may be a wind blown bubble by massive stars at the centre of the cluster. Visual estimation of radius of the bubble from Fig. 22 yields a value of  $\sim 13\text{--}14$  arcmin corresponding to 12–13 pc at the distance of NGC 1893. A stellar wind of power  $L_w \text{ erg s}^{-1}$  from a star located in a uniform cloud of neutral hydrogen density,  $n_0$  atoms  $\text{cm}^{-3}$ , will in time ' $t$ ' yr produce a spherical shell of diameter  $D(t)$  pc, expanding at  $V(t)$   $\text{km s}^{-1}$ , where

$$L_w = 9.5 \times 10^{17} n_0 V(t)^5 t^2,$$

$$D(t) = 3.5 \times 10^{-6} V(t) t \text{ (cf. Pandey et al. 2000)}.$$

Assuming that O7 stars at the centre of the cluster are injecting a kinetic energy  $L_w \sim 10^{36} \text{ erg s}^{-1}$ , with the gas density  $10^3\text{--}10^4 \text{ cm}^{-3}$  and age of O-type stars  $\sim 4$  Myr, the radius of the bubble corresponds to  $\sim 10\text{--}16$  pc.

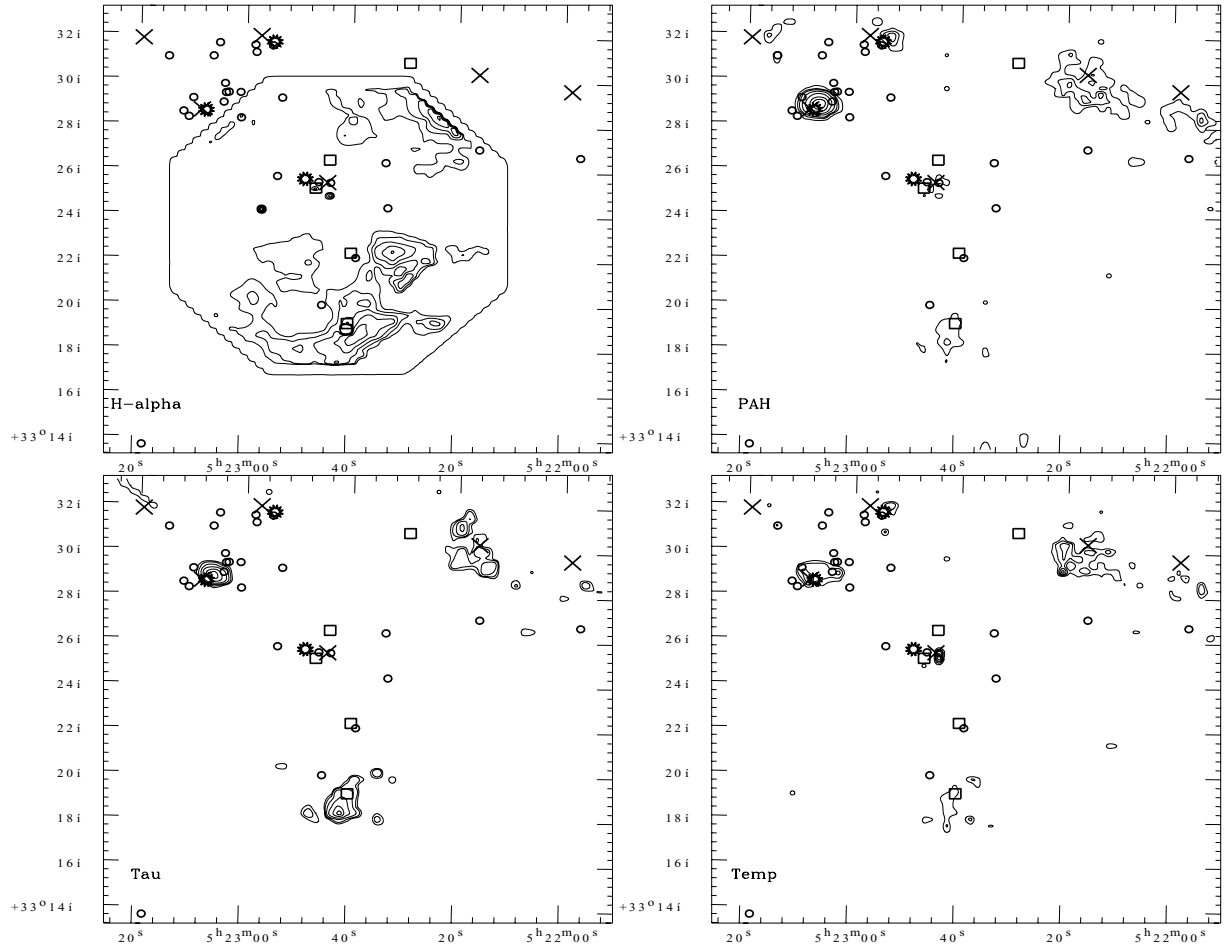


**Figure 25.**  $H\alpha$  intensity contours (top left); hexagon represents the area of  $H\alpha$  observations. Emission in UIBs (top right), distribution of optical depth ( $\tau_{10}$  at  $10\ \mu\text{m}$ ) (bottom left) and the distribution of dust temperature (bottom right) around the cluster region. The contours are at 1, 3, 5, 10, 20, 40, 60, 80 per cent of the peak value of  $2.7 \times 10^{-5}\ \text{W m}^{-2}\ \text{sr}^{-1}$  for UIBs; 3, 5, 10, 20, 40, 60, 80 per cent of the peak value of  $8.5 \times 10^{-5}$  for  $\tau_{10}$  and 20, 30, 40, 50, 60, 70, 80, 90 per cent of the peak value of 388 K for dust temperature. The symbols are same as in Fig. 22. The star symbols are the cluster centre and positions of two nebulae, i.e. Sim 129 and 130. The abscissa and the ordinates are in the J2000.0 epoch.

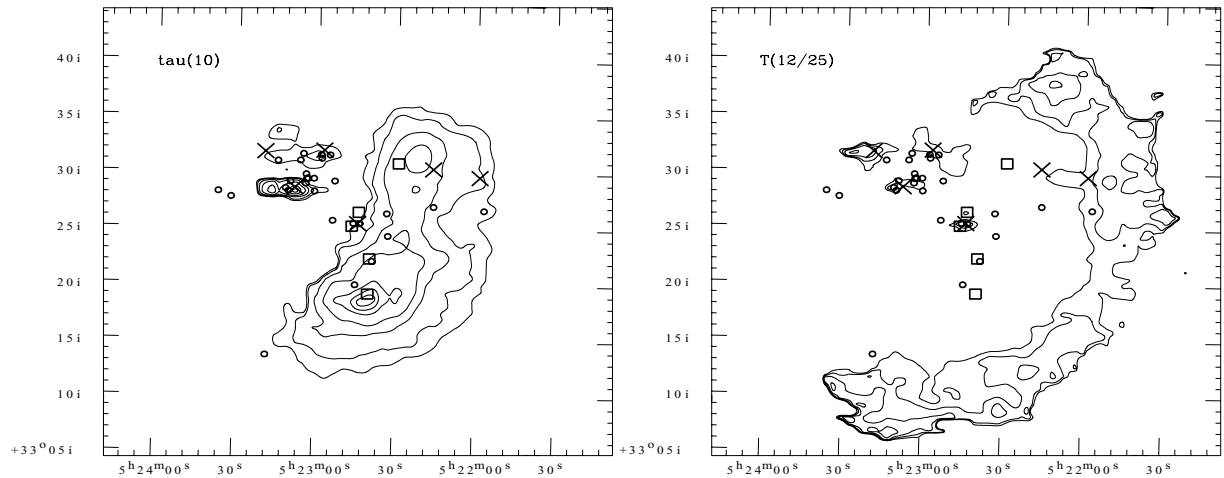


**Figure 26.** Left: the dust optical depth ( $\tau_{10}$ ) distribution from the HIRCS 12- and 25- $\mu\text{m}$  maps, scaled to  $10\ \mu\text{m}$  by  $\lambda^{-1}$  emissivity law. Right: colour temperature ( $T(12/25)$ ) maps of the region around the cluster. The optical depth contours are 3, 5, 10, 20, 40, 60, and 80 per cent of the peak value of  $1.35 \times 10^{-5}$ . The dust temperature contour levels are at 160, 171, 183, 197, 211, 226, 243, 260 and 279 K. The peak value is 300 K.

## 14 SUMMARY AND CONCLUSION

On the basis of a comprehensive multiwavelength study of the star-forming region NGC 1893 we have made an attempt to study the effects of massive stars on low mass star formation. Deep optical *UBVRI* and narrow band  $H\alpha$  photometric data, slitless spectroscopy along with archival data from the surveys such as 2MASS, MSX, *IRAS* and NVSS are used to understand the global scenario of star formation in and near the cluster region.

Reddening ( $E(B - V)$ ) in the direction of cluster is found to be varying between 0.40 and 0.60 mag. The post-MS age and distance of the cluster are found to be  $\sim 4$  Myr and  $3.25 \pm 0.20$  kpc, respectively. Using the NIR TCD and excess  $H\alpha$  emission we identified candidate YSOs which are aligned from the cluster to the direction of nebula Sim 129. The O-type stars at the centre of the cluster may be responsible for the trigger of star formation in the region. The morphology of the cluster seems to be influenced by the star formation in the region. We find a population of PMS YSOs in the cluster region having mass  $\sim 1-3.5 M_{\odot}$ . The position of the YSOs on the CMDs indicates that the majority of these stars have age between  $\sim 1$  and 5 Myr indicating a possibility of non-coeval star formation in the cluster. Two probable HBe stars in the vicinity of central O-type stars further indicate a prolonged star formation in the centre of the cluster region.

The KLF for the cluster is found to be  $0.34 \pm 0.07$  which is consistent with the average value ( $\sim 0.4$ ) obtained for young star clusters (Lada et al. 1991; Lada & Lada 1995, 2003). The slope of the IMF ‘ $\Gamma$ ’ for PMS stars (mass range  $0.6 < M/M_{\odot} \leq 2.0$ ) is found to be  $-0.88 \pm 0.09$ , which is shallower than the value ( $-1.71 \pm 0.20$ ) obtained for MS stars having mass range  $2.5 < M/M_{\odot} \leq 17.7$ . However, for the entire mass range ( $0.6 < M/M_{\odot} \leq 17.7$ ) the ‘ $\Gamma$ ’ comes out to be  $-1.27 \pm 0.08$ . The effect of mass segregation can be seen on the MS stars. The estimated dynamical evolution time is found to be greater than the age of the cluster, therefore, the observed mass segregation in the cluster may be the imprint of the star formation process.

## ACKNOWLEDGMENTS

Authors are thankful to the anonymous referee for useful comments. The observations reported in this paper were obtained using the 2-m HCT at IAO, Hanle, the high altitude station of Indian Institute of Astrophysics, Bangalore. We thank the staff at IAO, Hanle, and its remote control station at CREST, Hosakote, for their assistance during observations. This publication makes use of data from the 2MASS, which is a joint project of the University of Massachusetts and the Infrared Processing and Analysis Centre/California Institute of Technology, funded by the National Aeronautics and Space Administration and the National Science Foundation. AKP is thankful to the National Central University, Taiwan, for the financial support during his visit to NCU. The support given by the DST (India) is also thankfully acknowledged.

## REFERENCES

Aumann H. H., Fowler J. W., Melnyk M., 1990, *AJ*, 99, 1674  
 Bertelli G., Bressan A., Chiosi C., Fagotto F., Nasi E., 1994, *A&AS*, 106, 275  
 Bertout C., Basri G., Bouvier J., 1988, *ApJ*, 330, 350  
 Bessell M. S., Brett J. M., 1988, *PASP*, 100, 1134  
 Brandl B. et al., 1996, *ApJ*, 466, 254  
 Carraro G., Vázquez R. A., Moitinho A., Baume G., 2005, *ApJ*, 630, L153

Chen W. P., Chen C. W., Shu C. G., 2004, *AJ*, 128, 2306  
 Chini R., Wargau W. F., 1990, *A&A*, 227, 213  
 Cohen J. G., Frogel J. A., Persson S. E., Ellias J. H., 1981, *ApJ*, 249, 481  
 Cuffey J., 1973, *AJ*, 78, 408  
 Dolan C. J., Mathieu R. D., 2002, *AJ*, 123, 387  
 Elmegreen B. G., Lada C. J., 1977, *ApJ*, 214, 725  
 Fischer P., Pryor C., Murray S., Mateo M., Richtler T., 1998, *AJ*, 115, 592  
 Fitzsimmons A., 1993, *A&AS*, 99, 15  
 Gaze V. F., Shajn G. A., 1952, *Izv. Krym. Astrofiz. Obs.*, 9, 52  
 Ghosh S. K., Ojha D. K., 2002, *A&A*, 388, 326  
 Ghosh S. K., Verma R. P., Rengarajan T. N., Das B., Saraiya H. T., 1993, *ApJS*, 86, 401  
 Herbig G. H., 1962, *Adv. Astron. Astrophys.*, 1, 47  
 Hillenbrand L. A., 1997, *AJ*, 113, 1733  
 Hillenbrand L. A., Strom S. E., Vrba F. J., Keene J., 1992, *ApJ*, 397, 613  
 Hoag A. A., Johnson H. L., Iriarte B., Mitchell R. I., Hallam K. L., Sharpless S., 1961, *Publ. US Nav. Obs.*, 17, 347  
 Huang F., Chen W. P., Hsiao W. S., 2006, *J. Taipei Astron. Museum*, 4, 27  
 Israel F. P., 1978, *A&A*, 70, 769  
 Johnson H. L., Morgan W. W., 1953, *ApJ*, 117, 313  
 Joshi Y. C., 2005, *MNRAS*, 362, 1259  
 Kaluzny J., Udalski A., 1992, *Acta Astron.*, 42, 29  
 King I., 1962, *AJ*, 67, 471  
 Koorneef J., 1983, *A&A*, 128, 84  
 Kroupa P., 2002, *Sci*, 295, 82  
 Lada C. J., Adams F. C., 1992, *AJ*, 393, 278  
 Lada E. A., Lada C. J., 1995, *AJ*, 109, 1682  
 Lada C. J., Lada E. A., 2003, *ARA&A*, 41, 57  
 Lada E. A., Evans N. J., II, Depoy D. L., Gatley I., 1991, *ApJ*, 371, 171  
 Landolt A. U., 1992, *AJ*, 104, 340  
 Leisawitz D., Bash F. N., Thaddeus P., 1989, *ApJS*, 70, 731  
 McNamara B. J., Sekiguchi K., 1986, *ApJ*, 310, 613  
 Marco A., Negueruela I., 2002, *A&A*, 393, 195  
 Marco A., Bernabeu G., Negueruela I., 2001, *AJ*, 121, 2075  
 Massey P., Lang C. C., Degioia-Eastwood K., Garmany C. D., 1995a, *ApJ*, 438, 188  
 Massey P., Johnson K. E., DeGioia-Eastwood K., 1995b, *ApJ*, 454, 151  
 Mathieu R. D., 1985, *Int. Astron. Union Symp.*, 113, 427  
 Mathieu R. D., Latham D. W., 1986, *AJ*, 92, 1364  
 Meyer M., Calvet N., Hillenbrand L. A., 1997, *AJ*, 114, 288  
 Moffat A. F. J., Vogt N., 1974, *Veroff. Astron. Inst. Ruhr-Univ. Bochum*, 2, 1  
 Negueruela I., Marco A., Israel G., Bernabeu G., 2007, preprint ([astro-ph/0703706](http://arxiv.org/abs/astro-ph/0703706))  
 Ojha D. K. et al., 2004a, *ApJ*, 608, 797  
 Ojha D. K. et al., 2004b, *ApJ*, 616, 1041  
 Pandey A. K., Bhatt B. C., Mahra H. S., Sagar R., 1989, *MNRAS*, 236, 263  
 Pandey A. K., Mahra H. S., Sagar R., 1992, *Bull. Astron. Soc. India*, 20, 287  
 Pandey A. K., Ogura K., Sekiguchi K., 2000, *PASJ*, 52, 847  
 Pandey A. K., Nilakshi, Ogura K., Sagar R., Tarusawa K., 2001, *A&A*, 374, 504  
 Pandey A. K., Upadhyay K., Nakada Y., Ogura K., 2003, *A&A*, 397, 191  
 Pandey A. K., Upadhyay K., Ogura K., Sagar R., Mohan V., Mito H., Bhatt H. C., Bhatt B. C., 2005, *MNRAS*, 358, 1290  
 Pandey A. K., Sharma S., Ogura K., 2006, *MNRAS*, 373, 255  
 Phelps R. L., Janes K. A., 1993, *AJ*, 106, 1870  
 Phelps R. L., Janes K. A., 1994, *ApJS*, 90, 31  
 Preibisch T., Zinnecker H., 1999, *AJ*, 117, 2381  
 Price S. D., Egan M. P., Carey S. J., Mizuno D. R., Kuchar T. A., 2001, *AJ*, 121, 2819  
 Robin A. C., Reyle C., Derriere S., Picaud S., 2003, *A&A*, 409, 523  
 Sagar R., Richtler T., 1991, *A&A*, 250, 324  
 Sagar R., Piskunov A. E., Miakutin V. I., Joshi U. C., 1986, *MNRAS*, 220, 383

- Sagar R., Miakutin V. I., Piskunov A. E., Dluzhnevskaja O. B., 1988, MNRAS, 234, 831
- Salpeter E. E., 1955, ApJ, 121, 161
- Schmidt-Kaler Th., 1982, in Schaifers K., Voigt H. H., Landolt H., eds, Landolt-Bornstein, Vol. 2b. Springer-Verlag, Berlin, p. 19
- Sharma S., Pandey A. K., Ogura K., Mito H., Tarusawa K., Sagar R., 2006, AJ, 132, 1669
- Siess L., Dufour E., Forestini M., 2000, A&A, 358, 593
- Spitzer L., Jr, Hart M. H., 1971, ApJ, 164, 399
- Stetson P. B., 1987, PASP, 99, 191
- Stetson P. B., 1992, in Warrall D. M., Biemesderfer C., Barnes J., eds, ASP Conf. Ser. Vol. 25, Astronomical Data Analysis Software and System I. Astron. Soc. Pac., San Francisco, p. 297
- Sung H., Chun M., Bessell M. S., 2000, AJ, 120, 333
- Tapia M., Costero R., Echevarria J., Roth M., 1991, MNRAS, 253, 649
- Vallenari A., Richichi A., Carraro G., Girardi L., 1999, A&A, 349, 825

This paper has been typeset from a  $\text{\TeX}/\text{\LaTeX}$  file prepared by the author.